

Dense planetary rings and the viscous overstability

Henrik N. Latter^{a,b,*}, Gordon I. Ogilvie^b

^a*LRA, École Normale Supérieure, 24 rue Lhomond, Paris 5, France*

^b*DAMTP, University of Cambridge, Wilberforce Rd, Cambridge CB3 0WA, United Kingdom*

Abstract

This paper examines the onset of the viscous overstability in dense particulate rings. First, we formulate a dense gas kinetic theory that is applicable to the Saturnian system. Our model is essentially that of Araki and Tremaine (1986), which we show can be both simplified and generalised. Second, we put this model to work computing the equilibrium properties of dense planetary rings, which we subsequently compare with the results of N -body simulations, namely those of Salo (1991). Finally, we present the linear stability analyses of these equilibrium states, and derive criteria for the onset of viscous overstability in the self-gravitating and non-self-gravitating cases. These are framed in terms of particle size, orbital frequency, optical depth, and the parameters of the collision law. Our results compare favourably with the simulations of Salo *et al.* (2001). The accuracy and practicality of the continuum model we develop encourages its general use in future investigations of nonlinear phenomena.

Key words: Planetary Rings, Collisional Physics

* Corresponding author.

Email addresses: `henrik.latter@lra.ens.fr` (Henrik N. Latter),
`gio10@cam.ac.uk` (Gordon I. Ogilvie).

1 Introduction

Of the many exciting spectacles delivered by *Cassini* images of complicated finescale structure in Saturn’s B-ring are some of the most beautiful and intriguing (Porco *et al.*, 2005). Irregular radial features on large scales, of some 10—100 km, have been associated with the B-ring since *Voyager*, but *Cassini* has revealed that irregular structure is characteristic of sub-kilometre scales as well. In fact, a recent analysis of the UVIS stellar occultation data has uncovered quasi-periodic variations on lengths as short as 150 m (Colwell *et al.*, 2007). It has been suggested that these phenomena correspond to the saturated state of the viscous overstability, as examined by Schmit and Tscharnuter (1995, 1999). The viscous overstability is a linear instability that occurs when the viscous stresses vary with density in such a way that energy from the Keplerian shear can be directed into growing oscillations. The most vigorously growing modes possess lengths of some 100—200 m and could very well be responsible for irregular structure on sub-kilometre scales. On the other hand, it is perhaps unlikely that this mechanism generates the much longer 100 km features first reported by *Voyager*, as had been originally hoped. These instead may be the responsibility of ballistic transport (Durisen, 1995) or electromagnetic effects (Goertz and Morfill, 1988). Lending weight to the overstability hypothesis are *Cassini* ISS observations which report that finescale structure favours regions in which the optical depth is greater (Figs 5A and 5B, Porco *et al.*, 2005); *N*-body simulations show the overstability is similarly sensitive to optical depth (Salo *et al.*, 2001). These new observations, and the theoretical challenges they throw up, encourage us to examine in greater detail when and why this instability occurs (its linear theory) and the manner in which it saturates (its nonlinear theory).

Researchers have mainly probed the onset of the instability with hydrodynamic models, sometimes allied with *N*-body simulations (Schmit and Tscharnuter, 1995; Spahn *et al.*, 2000; Salo *et al.*, 2001; Schmidt *et al.*, 2001). In addition, Schmit and Tscharnuter (1999) have conducted nonlinear hydrodynamical simulations and Schmidt and Salo (2003) a weakly nonlinear analysis, both with isothermal models. The former study shows that the overstability takes the system into a disordered state in which power is transferred to longer and longer wavelengths, a process that only saturates if self-gravity is present. Schmit’s and Tscharnuter’s adoption of reflecting boundary conditions, however, prohibits the development of the stable nonlinear travelling wave solutions that Schmidt and Salo (2003) discover. If dense regions of the B-ring indeed favour the nonlinear wave solution these probably possess a wavelength below the resolution of *Cassini*’s cameras but can be captured by the UVIS or RSS instruments: in fact, it is very likely that the significant 150 m structures reported by the UVIS correspond to these nonlinear waves. Perhaps we can then interpret the irregular structure observed on slightly longer scales

(1—10 km) as largescale modulations of the wave trains’ amplitudes and/or wavenumbers, by analogy with water-waves and flame-fronts (Infeld and Rowlands, 1990), or alternatively they may correspond to ‘defects’ between wave trains of differing properties, by analogy with the dynamics of the complex Ginzberg-Landau equation (Aranson and Kramer, 2002). Certainly there is a lot of interesting work to be done examining the nonlinear aspects of this problem.

In this paper, however, we shall reconsider the onset of the viscous overstability in a dense ring. We employ a kinetic theory, and hence extend the dilute ring analysis of Latter and Ogilvie (2006). In that study it was argued that hydrodynamical models fail to capture important effects associated with the velocity anisotropy and non-Newtonian stress. Both we predict will play a part in the dynamics of a dense ring as well, a concern which motivates our adoption of the better-suited kinetic approach. Moreover, a kinetic model can be framed in terms of parameters (particle size, collisional parameters, etc) that can be constrained by observation or experiment. This parameterisation also makes a comparison with N -body simulations unproblematic. In contrast, hydrodynamics must make (sometimes speculative) prescriptions for the transport coefficients, because their functional dependence on the observables is unclear.

The price one pays for using a kinetic model is mathematical complexity. The dense gas collision terms are especially troublesome as they usually consist of complicated multi-dimensional integrals. Consequently, a number of assumptions are necessary to obtain some mathematical purchase on the problem. The model we employ is the one developed by Araki and Tremaine (1986) (hereafter referred to as AT86), which assumes that the distribution function is a triaxial Gaussian. Such a distribution enabled Araki and Tremaine to reduce the collision integrals to four dimensions. In this paper we show that further integrations are possible even when the coefficient of restitution is allowed to depend on normal impact velocity. In fact, if certain additional approximations are made, the remaining integrals can be executed by hand. These simplifications greatly facilitate the computation of the equilibrium states (previously a difficult numerical problem), and also open the way for more advanced analyses: with the elimination of these mathematical obstacles, a kinetic theory can be applied more generally, particularly to nonlinear behaviour that is presently beyond the range of direct N -body simulations.

In many ways, this work is similar to that of Hämeen-Anttila who in a suite of papers developed the statistical mechanics of orbital elements using many of the same approximations and techniques (see Hämeen-Anttila and Salo, 1993, and references therein). The results derived using these methods should coincide with ours, though we find that working in a shearing sheet with a phase space of velocity and location elucidates local instabilities (such as the viscous overstability) much more clearly.

The format of the paper is as follows. The rest of this section introduces the viscous overstability and sketches out the basic issues pertinent to modelling a dense gas. In Section 2 we develop a dense ring model — some of this section draws on previous work by Jenkins and Richman (1985) and AT86. Section 3 presents calculations and discussions of dense ring equilibria plus a comparison with the N -body simulations of Wisdom and Tremaine (1988) and Salo (1991). In Section 4 we undertake a linear stability analysis of these states, thereby obtaining criteria for the onset of viscous overstability in the non-self-gravitating and self-gravitating cases. These results we compare with Salo *et al.* (2001). In Section 5 we draw our conclusions and point out future work.

1.1 *The viscous overstability*

The viscous overstability is one of two instabilities of viscous origin that have been proposed to explain structure in planetary rings. The other, the viscous instability, occurs wherever the outward angular momentum flux is a decreasing function of surface density, a situation that initiates a clumping of matter into ringlets (Lin and Bodenheimer, 1981; Ward, 1981; Lukkari, 1981). For plausible parameters, the angular momentum flux of dense rings has been shown to be an *increasing* function of surface density (Araki and Tremaine, 1986; Wisdom and Tremaine, 1988), and so it is unlikely that this instability occurs in Saturn’s dense rings.

The viscous overstability, on the other hand, emerges from a Hopf bifurcation and, as the name suggests, can be characterised as an overcompensation by the system’s restoring forces: the stress oscillation which accompanies the epicyclic response in an inertial-acoustic wave will force the system back to equilibrium so strongly that it will ‘overshoot’. Without self-gravity the longest lengthscales are the most susceptible to this runaway process, though they will grow slowly because the waves’ growth rate is proportional to k^2 , where k is radial wavenumber. For sufficiently small wavelengths, pressure extinguishes the instability and so there is a preferred intermediate scale upon which the viscous overstability grows most vigorously. When self-gravity is added the disk is more unstable, particularly on a band of intermediate wavelengths.

The mechanism of overstability relies on: a) the synchronisation of the viscous stress’ oscillations with those of density, and b) the viscous stress increasing sufficiently steeply with surface density. In hydrodynamics only the latter consideration is relevant, which furnishes the criterion for overstability:

$$\beta \equiv (d \ln \nu / d \ln \sigma) > \beta^*,$$

where ν is viscosity, σ is surface density, and β^* is a number dependent on the

thermal properties of the ring (Schmit and Tscharnuter, 1995). Generally, the viscous stress need not oscillate in phase with the inertial-acoustic wave, in which event the transfer of energy between the two oscillations can be quite inefficient: usually the potential overstable modes are damped as a consequence. This is what happens in dilute particulate rings at small and intermediate collision frequencies (Latter and Ogilvie, 2006). The viscous stress of such rings, being predominately local (or ‘translational’), possesses a relaxation time of order the dynamical time scale, and so they lag behind the epicyclic variations. In contrast, the viscous stress in a dense ring is dominated by the nonlocal (‘collisional’) component which oscillates in phase with the inertial motion. Moreover, the effective viscosity profiles computed by AT86’s dense gas model and Wisdom and Tremaine’s (1988) particle simulations display a relatively steep increase with optical depth (hence σ), suggesting that the effective β of the system may be sufficiently large to instigate overstability.

As a consequence, the linear behaviour of the viscous overstability has been thoroughly examined, mainly with hydrodynamics (in the papers mentioned earlier). However, it is upon the N -body study of Salo *et al.* (2001) that we will concentrate. There the collisional evolution of 100 cm radius particles were tracked in a shearing box situated in the B-ring undergoing collisions that dissipate energy in accordance with the piecewise power law:

$$\varepsilon(v_n) = \begin{cases} (v_n/v_c)^{-p}, & \text{for } v_n > v_c, \\ 1, & \text{for } v_n \leq v_c, \end{cases} \quad (1)$$

where ε is the coefficient of restitution and v_n is normal impact speed. The parameters p and v_c took the values deduced from the ice-collision experiments of Bridges *et al.* (1984), specifically: $p = 0.234$ and $v_c = 0.0077 \text{ cm s}^{-1}$. These simulations show that a dense non-self-gravitating disk is stable for all optical depths below about four¹. This critical value is reduced to about one if self-gravity’s enhancement of the vertical restoring force is included. If self-gravity is fully modelled the emergence of the overstability is somewhat retarded by the vigorous percolation of non-axisymmetric gravitational wakes, because these motions modify the effective viscous properties of the system.

It is problematic to obtain a general criterion for overstability from simulations in terms of the various parameters, as this would require a great number of individual runs. Moreover, the fluid dynamical criterion cannot be neatly related to the N -body results, the main problem being that the quantities involved, namely ν and β^* , are not straightforward functions of the N -body, or observable, parameters (particle size, orbital frequency, etc). Some of the hydrodynamic quantities can be numerically obtained for a particular equilibrium state

¹ Throughout this paper ‘optical depth’ will denote normal geometric optical thickness.

using simulations (Salo *et al.*, 2001; Schmidt *et al.*, 2001), but the role of the various observable parameters is difficult to bring out, as these fluid dynamical quantities are tied to the particulars of a specific (and lengthy) computation. That said, some of the appurtenant results so obtained (growth/decay rates mainly) are in good agreement with the simulations, even if the assumptions implicit in a hydrodynamic model possibly lead to errors.

We seek to use kinetic theory to remedy this problem, by providing a criterion for the onset of overstability, specifically an estimate of the critical optical depth τ_c , as a function of the kinetic parameters of the system, which connect to the observable data: particle radius a , particle mass m , local orbital frequency Ω , and the parameters that appear in the elasticity law.

1.2 Dense gases

It was not until the late 1980s that it was fully appreciated that nonlocal ‘dense’ effects were critical and widespread in Saturn’s rings. Perhaps this shift was initiated most by the theoretical papers of AT86 and Araki (1988, 1991), and the simulations of Wisdom and Tremaine (1988) and Salo (1991). In fact, the issue had been presaged by Brahic (1977) and examined in some detail by Hämeen-Anttila (1982) and Shukhman (1984). Essentially, Araki and Tremaine and Wisdom and Tremaine revealed that (a) collisional contributions are crucial to the equilibrium when collisions are sufficiently inelastic and (b) the experimentally derived elasticity laws of (1) predict that collisions are dissipative enough for this ‘cold’ regime to be ubiquitous in Saturn’s rings, given appropriate particle sizes (Marouf *et al.*, 1983; Zebker *et al.*, 1985). In addition, both simulations and theoretical models show that the dynamics of small particles (for which nonlocal effects are less important) strongly couples to the dynamics of the largest particles (for which nonlocal effects are important) both in two-size systems and in polydisperse disks exhibiting power-law size distributions akin to Saturn’s (Stewart *et al.*, 1984; Lukkari, 1989; Salo, 1987, 1991, 1992b).

To capture theoretically this dense regime we turn to the Enskog model which revises the Boltzmann theory for moderately dense gases (Chapman and Cowling, 1970). The Enskog formalism distinguishes two additional processes not captured by Boltzmann kinetics; the first is associated with a large filling factor, where filling factor (FF) denotes the proportion of space occupied by particles and is defined, for spheres, through

$$\text{FF} \equiv \frac{4}{3}\pi n a^3,$$

where n is volumetric number density and a is particle radius. The second process is associated with the collisional transfer of particle properties such as

momentum and energy. We describe these in turn.

When particles take up a significant portion of space (i.e. when FF is not small) the volume in which they may move is reduced, and possible colliders may be screened by other particles (Chapman and Cowling, 1970). This means that the statistics of two impacting particles must include the influence of their neighbours and, as a consequence, the evaluation of the collision frequency must take space correlations into account. Overall, this leads to an enhancement of the collision frequency ω_c which, in the Enskog theory, is approximately quantified by a factor $Y(\text{FF})$ (the ‘Enskog factor’). This cannot be calculated within the bounds of kinetic theory but must be determined separately, usually from data gathered in molecular dynamics experiments (Araki and Tremaine, 1986; Jenkins and Richman, 1984; Pöschel and Brilliantov, 2004). Inelastic and spinning systems may differ in this respect from their elastic and spinning counterparts because they can develop postcollisional correlations in their particles’ tangential velocity. Inelastic collisions diminish the normal component of the relative velocity but conserve the tangential component, and as a result subsequent collisions lead to a statistical alignment of neighbouring particles’ traces (Brilliantov and Pöschel, 2004). Other than possibly forming vortices, this effect can reduce the local value of the collision frequency, and so the Enskog factor of an inelastic ensemble may be smaller than that of a corresponding elastic system (see Pöschel, Brilliantov and Schwager, 2002). That all said, in ring applications the net effect seems negligible.

There are two ways properties may be transferred in a particle gas: their free carriage by particles *between* collisions and their transmission from one particle to another *during* a collision. In a dilute gas, the former so-called ‘local’, or translational, mode dominates the latter because particles travel relatively long distances between collisions. In a dense gas, the mean free path is much reduced and can approach a particle radius, in which case the finite size of the particles is sufficiently large for the exchange of properties between colliding particles to compete with, or even dominate, translational transport. Estimates for the relative magnitude of the two types are easy to derive. Consider the transport of momentum across a plane by a gas characterised by mass density ρ and velocity dispersion c , and composed of particles of radius a . The magnitude of the momentum flux density due to the free carriage of particles is of order ρc^2 . On the other hand, the flux density of momentum carried in collisions from the centres of all the particles on one side of the surface to all the particles on the other side is of order $(\rho c)a\omega_c$. This implies the scaling:

$$\frac{\|\mathbf{p}^c\|}{\|\mathbf{p}^t\|} \sim \frac{a\omega_c}{c} = (\omega_c/\Omega)R, \quad (2)$$

where \mathbf{p}^c and \mathbf{p}^t refer to the collisional and translational pressure tensors

respectively, Ω is the local orbital frequency, and R is defined by

$$R \equiv \frac{a\Omega}{c}. \quad (3)$$

Elsewhere R is called the Savage and Jeffrey R -parameter (Savage and Jeffrey, 1981; Araki, 1991), and it quantifies the ratio of shear motions to velocity dispersion. Here Ω is a substitute for shear rate. Note that it is $(\omega_c/\Omega)R$ that quantifies the importance of collisional transport in the ring *dynamics*. In contrast, an analogous argument shows that R^2 quantifies the importance of collisional effects in the ring *energetics*: because heating and cooling are proportional to collision frequency the ω_c/Ω can be dropped from the estimate.

The effects of large filling factor and collisional transport usually work in tandem, though for very high or very low optical depths there are cases when one can exist without the other. This is expressed in the scaling:

$$\tau \sim \text{FF}/R. \quad (4)$$

For a substantial discussion on this subject see Araki (1991). In Saturn's rings R is probably of order unity (Salo, 1992b), which means that filling factor effects are as important as the optical depth is large. In low optical depth regions, such as the C and D-rings and the Cassini division, filling factor effects are hence negligible. In contrast, collisional transport/production effects will be important throughout the rings on account of their low velocity dispersion ($R \sim 1$).

Kinetic models and N -body simulations, in order to make any progress, must introduce a number of simplifying assumptions. Typically, ring particles are taken to be identical, perfectly smooth, hard, indestructible spheres which dissipate energy in collisions according to a simple 'elasticity law' such as (1) (the 'billiard ball' model). Though these presumptions facilitate calculations, it is unclear how appropriate some of these are to the real rings of Saturn. Neglecting spin and size-distribution should give qualitatively correct results for those particles which dominate the dynamics (near 100 cm size). Also it is plausible that the timescale of the size dynamics (erosion and accretion, etc) may be much larger than the dynamical timescale (Ω^{-1}), meaning these processes do not interfere with the instabilities we study. In any case, the modelling of spin is hampered by the fact that the frictional properties of the ice particles are poorly constrained. We admit that 'smoothing' over the complicated details of an actual collision with a simple ε law is a bold approximation, particularly as there is considerable uncertainty about the relevant physics for real ring particles. A number of terrestrial experiments, however, have been conducted with solid ice spheres (Bridges *et al.*, 1984; Hatzes *et al.*, 1988; McDonald *et al.*, 1989; Hatzes *et al.*, 1991; Supulver *et al.*, 1995; Supulver *et al.*, 1997). These show that the coefficient of restitution varies considerably as

the physical condition of the contact surface is frosty, sintered, or sublimated. Depending on the surface condition, various processes ensue, such as erosion, sticking, mass transfer, and regolith compactification, all of which influence ε . But it has also been suggested that a particle may resemble more of a rubble pile (a ‘dynamic ephemeral body’) held together by mutual gravitation (Weidenschilling *et al.*, 1984) and/or adhesion (Albers and Spahn, 2006), in which case the collisional dynamics will be very different — and the assumption of ‘hardness’, and a neat ε law itself, perhaps unsupportable. Unfortunately, we lack detailed information about the physical state of a ring particle, and given this uncertainty assume that laws such as (1) capture the correct qualitative behaviour, though the parameters which appear in them may be subject to much variability.

2 The kinetic model

2.1 Governing equations

Consider a gas of indestructible identical nonspinning inelastic spheres of mass m and radius a , and with phase space distribution $f(\mathbf{x}, \mathbf{v}, t)$. The number of particles located in the volume $d\mathbf{x}$ centred at \mathbf{x} with velocities in the range $d\mathbf{v}$ centred at \mathbf{v} at time t is defined as $f(\mathbf{x}, \mathbf{v}, t)d\mathbf{x}d\mathbf{v}$. Number density n , bulk velocity \mathbf{u} , and the pressure tensor p_{ij} are defined, consequently, through

$$n(\mathbf{x}, t) \equiv \int f d\mathbf{v}, \quad (5)$$

$$nu_i(\mathbf{x}, t) \equiv \int v_i f d\mathbf{v}, \quad (6)$$

$$p_{ij}(\mathbf{x}, t) \equiv \int (v_i - u_i)(v_j - u_j) f d\mathbf{v}. \quad (7)$$

The phase space distribution satisfies a kinetic equation which is distinguished by a collision operator, $(\partial f / \partial t)_c$, whose precise form reflects the collisional microphysics. This equation is presented after we describe the geometry of the problem.

The particle gas inhabits the shearing sheet (see Goldreich and Lynden-Bell, 1965). This is a convenient representation of a differentially rotating disk in which a small patch, centred on a point moving on a circular orbit at $r = r_0$, is represented as a sheet in uniform rotation, $\Omega(r_0) \mathbf{e}_z$, and subject to a linear shear flow, $\mathbf{u}_0 = -2A_0 x \mathbf{e}_y$. The local rectilinear coordinates x and y point in the radial and azimuthal directions respectively and $A_0 = -\frac{1}{2}r_0(d\Omega/dr)_0$. A Keplerian disk requires $A_0 = \frac{3}{4}\Omega_0$, where $\Omega_0 = \Omega(r_0)$. This approximation is valid if the radial wavenumber of typical variations k satisfies $|kr_0| \gg 1$, which

is certainly the case for the phenomenon of interest. From now the subscript ‘0’ will be dropped.

In terms of the peculiar velocity, $\mathbf{w} \equiv \mathbf{v} - \mathbf{u}$, the kinetic equation for particles in the shearing sheet is

$$\frac{\partial f}{\partial t} + (w_i + u_i) \frac{\partial f}{\partial x_i} - \left[\frac{\partial u_i}{\partial t} + (w_j + u_j) \frac{\partial u_i}{\partial x_j} - F_i \right] \frac{\partial f}{\partial w_i} = \left(\frac{\partial f}{\partial t} \right)_c, \quad (8)$$

where the force per unit mass is

$$F_i = -\frac{\partial(\phi_P + \phi_D)}{\partial x_i} - 2\epsilon_{ijk}\Omega_j(w_k + u_k).$$

The appropriate centrifugal-gravitational potential of the planet is denoted by ϕ_P and the disk’s gravitational potential by ϕ_D . The tensor ϵ_{ijk} is the alternating tensor and the angular velocity is $\boldsymbol{\Omega} = \Omega \mathbf{e}_z$. By multiplying (8) by 1, w_i and $w_i w_j$ and then integrating over all \mathbf{w} we derive the continuity equation,

$$\partial_t n + \partial_k(nu_k) = 0, \quad (9)$$

the equation of motion,

$$n(\partial_t u_i + u_k \partial_k u_i) = -2n\epsilon_{ijk}\Omega_j u_k - n\partial_i(\phi_P + \phi_D) - \partial_j p_{ij} + m_i, \quad (10)$$

and the pressure tensor equation,

$$\begin{aligned} \partial_t p_{ij} + u_k \partial_k p_{ij} = & -p_{ik} \partial_k u_j - p_{jk} \partial_k u_i - p_{ij} \partial_k u_k - 2\epsilon_{ikl}\Omega_k p_{lj} \\ & - 2\epsilon_{jkl}\Omega_k p_{li} - \partial_k p_{ijk} + q_{ij}, \end{aligned} \quad (11)$$

where p_{ijk} is the third-order moment,

$$p_{ijk} = \int w_i w_j w_k f d\mathbf{w}, \quad (12)$$

the collisional change in the first moment is

$$m_i = \int w_i \left(\frac{\partial f}{\partial t} \right)_c d\mathbf{w}, \quad (13)$$

and the collisional change in the second moment is

$$q_{ij} = \int w_i w_j \left(\frac{\partial f}{\partial t} \right)_c d\mathbf{w}. \quad (14)$$

For notational brevity we have set $\partial_i = \partial/\partial x_i$. If nonlocal transport effects are neglected then m_i is zero on account of momentum conservation. Jenkins and Richman (1985) show how to rewrite this term as a flux, so that

$$m_i = -\partial_j p_{ij}^c,$$

where p_{ij}^c is the collisional pressure tensor. We will work with this form for the rest of this paper.

The moment equations are vertically integrated, a task that is easily performed once we assume that u_x , u_y , and p_{ij} are independent of z . Thus the disk is assumed to be vertically isothermal. In addition, vertical averaging permits us to close the hierarchy of the moment equations. In the pressure tensor equation Eq. (11), this procedure removes the dominant z derivatives of the third-order moment, $\partial_z p_{ijk}$, leaving only its horizontal derivatives, which scale relative to the other terms like Hk , where H is disk semithickness and k is the wavenumber of a typical horizontal variation. We expect these variations to be much longer than the disk thickness and so treat these flux terms as negligible. In summary, the closed governing equations we derive validly describe behaviour on scales satisfying $H \ll \lambda \ll r_0$, where λ is wavelength.

We define optical depth as $\tau \equiv \pi a^2 N$, where N is surface number density. We also introduce the velocity dispersion tensor:

$$W_{ij} \equiv p_{ij}/n.$$

This then allows the vertically-averaged equations to be recast as

$$D_t \tau = -\tau \partial_\alpha u_\alpha, \quad (15)$$

$$D_t u_\alpha = -\partial_\alpha (\Phi_P + \Phi_D) - 2\epsilon_{\alpha\beta\gamma} \Omega u_\beta - \frac{1}{\tau} \partial_\beta [\tau W_{\alpha\beta} + \tau P_{\alpha\beta}^c/N], \quad (16)$$

$$D_t W_{ij} = -W_{jk} \partial_k u_i - W_{ik} \partial_k u_j - 2\epsilon_{izk} \Omega W_{kj} - 2\epsilon_{jzk} \Omega W_{ki} + Q_{ij}/N, \quad (17)$$

where $D_t = \partial_t + u_\gamma \partial_\gamma$, Greek indices run only from x to y and upper case denotes vertical integration except for Φ_P and Φ_D which are vertically averaged (if needed). We approximate the central body as perfectly spherical, which accounts for the former potential, as then $\Phi_P = 3\Omega^2 x^2/2 + \mathcal{O}(x/r_0)$. This is acceptable because the precessional effects associated with planetary oblateness are unimportant for the instabilities we study. The latter potential Φ_D must be obtained from Poisson's equation:

$$\nabla^2 \phi_D = 4\pi m G n, \quad (18)$$

where G is the gravitation constant

Finally, we are left with the vertical component of the equation of motion from which it is possible to extract an equation for the mean vertical displacement of the disk Z (see Shu and Stewart, 1985). In this paper we do not investigate vertical warping of the disk. We assume vertical hydrostatic equilibrium and symmetry about the plane $z = 0$; thus $Z = P_{xz} = P_{yz} = 0$. The vertical

balance furnishes an equation for the vertical stratification of density

$$-\Omega^2 z - 4\pi G n m \int_0^z n(\hat{z}) d\hat{z} - \partial_z [nW_{zz} + P_{zz}^c] = 0. \quad (19)$$

This integro-differential equation for n can be manipulated into a second order ODE, which must be solved concurrently with Eqs (15)–(17). Alternatively, an ansatz for the form of n can be employed, such as a Gaussian (AT86) or a polytrope (Borderies, Goldreich and Tremaine, 1985; Mosquera, 1996), in which case (19) becomes an algebraic equation for either the scale height or semithickness of the disk, H .

The assumption of vertical hydrostatic equilibrium, though convenient, may be inappropriate when dealing with many dynamical phenomena, including overstable oscillations and density waves. This is because the timescale upon which vertical equilibrium is established should be of the same order as the dynamical time. It is possible to derive a dynamical equation for H , which could capture this effect. But for simplicity we persist with the hydrostatic model in this paper.

2.2 Construction of the collision integrals

In the dilute disk analysis of Latter and Ogilvie (2006) the microphysical details of the collisional interactions could be largely sidestepped by adopting a BGK model (Shu and Stewart, 1985; Bhatnagar, Gross and Krook, 1954). The collision terms in this case were simple, analytic, and local in space. Regrettably, no comparable approximation exists for the nonlocal collisional interactions of a dense gas. Hence we wade into the mathematics of the Boltzmann-Enskog collision theory and build the terms q_{ij} and p_{ij}^c from first principles. In their construction it will be assumed that particles only interact with each other through collisions and not also through gravity. This omission eliminates the possibility of gravitational focusing and scattering.

2.2.1 The kinematics of binary collisions

In order to ascertain the consequences of particle collisions collectively we must establish the basic physics of a single collision first. Consider two colliding particles of mass m and radius a travelling with velocities \mathbf{v}_1 and \mathbf{v}_2 immediately before the collision and \mathbf{v}'_1 and \mathbf{v}'_2 immediately afterwards. The relative velocities pre and postcollision are $\mathbf{g} = \mathbf{v}_1 - \mathbf{v}_2$ and $\mathbf{g}' = \mathbf{v}'_1 - \mathbf{v}'_2$, and their locations at the moment of collision are \mathbf{x}_1 and \mathbf{x}_2 . The collision is assumed to be inelastic and so the component of \mathbf{g} normal to the impact is

reduced by the factor ε , the coefficient of restitution. Hence we write

$$\mathbf{g}' \cdot \mathbf{k} = -\varepsilon \mathbf{g} \cdot \mathbf{k}$$

where \mathbf{k} is the unit vector directed from the centre of particle 1 to that of particle 2 so that

$$\mathbf{x}_2 - \mathbf{x}_1 = 2a \mathbf{k}.$$

Obviously, $\mathbf{g} \cdot \mathbf{k} > 0$ (the impact velocity cannot be negative). Also, it is assumed that ε is a function of normal impact velocity, $v_n \equiv \mathbf{g} \cdot \mathbf{k}$.

This prescription is sufficient to set the postcollisional velocities:

$$\mathbf{v}'_1 = \mathbf{v}_1 - \mathbf{j}, \quad \mathbf{v}'_2 = \mathbf{v}_2 + \mathbf{j}, \quad (20)$$

where

$$\mathbf{j} = \frac{1}{2}(1 + \varepsilon)(\mathbf{g} \cdot \mathbf{k})\mathbf{k},$$

and $m\mathbf{j}$ is the momentum transferred from particle 1 to particle 2.

The velocity of a particle may be expressed as the sum of the local mean velocity $\mathbf{u}(\mathbf{x}, t)$ and the peculiar velocity of the particle, $\mathbf{w} = \mathbf{v} - \mathbf{u}$. The precollisional relative velocity is therefore

$$\mathbf{g} = \mathbf{w}_1 - \mathbf{w}_2 + \mathbf{h},$$

where \mathbf{h} denotes the difference in mean velocity between the locations of the particles: thus $\mathbf{h} \equiv \mathbf{u}(\mathbf{x}_1, t) - \mathbf{u}(\mathbf{x}_2, t)$. Since the collision is instantaneous the mean velocity does not change in the collision, and because the particles are assumed perfectly smooth, the tangential component of \mathbf{g} is conserved.

The prescription above determines the total change in the peculiar velocity dyadic in a binary collision,

$$\begin{aligned} \Delta(\mathbf{w}\mathbf{w}) &= \mathbf{w}'_1\mathbf{w}'_1 + \mathbf{w}'_2\mathbf{w}'_2 - \mathbf{w}_1\mathbf{w}_1 - \mathbf{w}_2\mathbf{w}_2 \\ &= \frac{1}{2}(1 + \varepsilon)(\mathbf{g} \cdot \mathbf{k})[(\mathbf{h} - \mathbf{g})\mathbf{k} + \mathbf{k}(\mathbf{h} - \mathbf{g}) + (1 + \varepsilon)(\mathbf{g} \cdot \mathbf{k})\mathbf{k}\mathbf{k}]. \end{aligned} \quad (21)$$

Hence the total change in peculiar kinetic energy is

$$\frac{1}{2} m \Delta(w^2) = -\frac{1}{4} m (1 - \varepsilon^2) (\mathbf{g} \cdot \mathbf{k})^2 + m \mathbf{j} \cdot \mathbf{h}. \quad (22)$$

The first term in (22) represents the dissipative loss of energy (zero when $\varepsilon = 1$). The second term represents the gain in energy from the transfer of momentum across the mean shear flow. If the particle size is sufficiently small so that $|\mathbf{h}| \ll |\mathbf{w}_1 - \mathbf{w}_2|$ (which corresponds loosely to $R \ll 1$, see Eq. (3)), then this contribution can be neglected.

2.2.2 The statistics of binary collisions

We now determine the frequency of a particular collision specified by \mathbf{v}_1 , \mathbf{v}_2 , \mathbf{x}_1 , and \mathbf{x}_2 . This requires the introduction of the pair distribution $f^{(2)}$ which is defined so that

$$f^{(2)}(\mathbf{v}_1, \mathbf{x}_1, \mathbf{v}_2, \mathbf{x}_2, t) d\mathbf{v}_1 d\mathbf{v}_2 d\mathbf{x}_1 d\mathbf{x}_2$$

is the probable number of particle pairs located in the small volumes $d\mathbf{x}_1$ and $d\mathbf{x}_2$ centred at \mathbf{x}_1 and \mathbf{x}_2 , with velocities in the volumes $d\mathbf{v}_1$ and $d\mathbf{v}_2$ centred at \mathbf{v}_1 and \mathbf{v}_2 in velocity space, at a time t . For a dilute gas, in which particles are well spaced and travel relatively long distances between collisions, we may appeal to the assumption of molecular chaos (*Stosszahlansatz*) in order to simplify the distribution. This assumption states that there exists no correlation between the velocities and positions of any two particles before their collision. Consequently, we write $f^{(2)}(\mathbf{v}_1, \mathbf{x}_1, \mathbf{v}_2, \mathbf{x}_2, t)$ as the product of two single particle distributions, $f(\mathbf{x}_1, \mathbf{v}_1, t)$ and $f(\mathbf{x}_2, \mathbf{v}_2, t)$. But in a dense gas the probable positions of two colliding particles will be influenced by the presence of their neighbours. As mentioned earlier, we may approximate this by including the Enskog factor Y , which we take as a function of filling factor, and hence number density, $n(\mathbf{x})$. This last assumption limits Y to express position correlations only and is justified for elastic gases in which number density is nearly uniform. As we only explore homogeneous equilibrium or small deviations from it, this aspect of the assumption is acceptable for our purposes (AT86). More generally, velocity or higher order correlations may need to be taken into account. In summary, we write for two identical particles of radius a in contact

$$f^{(2)}(\mathbf{v}_1, \mathbf{x}_1, \mathbf{v}_2, \mathbf{x}_1 + 2a\mathbf{k}, t) = Y[n(\mathbf{x}_1 + a\mathbf{k})]f(\mathbf{v}_1, \mathbf{x}_1, t)f(\mathbf{v}_2, \mathbf{x}_1 + 2a\mathbf{k}, t). \quad (23)$$

In the limit of vanishing filling factor the Enskog factor approaches unity, and we recover the *Stosszahlansatz*. In the opposite limit, when particles are so densely packed that random movement is impossible, Y diverges. This occurs when FF = 0.74 for a collection of identical spheres arranged in a face-centred cubic lattice (AT86).

The Enskog factor cannot be calculated from within the compass of kinetic theory, but a number of expressions for it have been derived when the kinetic gas is elastic, non-shearing, and possessing a small filling factor (Ree and Hoover, 1967; Carnahan and Starling, 1969; Devore, 1984). This paper employs for Y the convenient interpolation of AT86 to the molecular dynamics data of Alder and Wainwright (Ree and Hoover, 1967). These details appear later.

We now present the collision frequency. Consider two particles with velocities \mathbf{v}_1 and \mathbf{v}_2 with the first located at \mathbf{x} . For a collision to occur characterised by a line of centres \mathbf{k} in the solid angle $d\mathbf{k}$, the second particle must be within a skew cylinder of volume $4a^2(\mathbf{g} \cdot \mathbf{k})d\mathbf{k}dt$. Therefore the frequency of a collision

between two particles with velocities in the volumes $d\mathbf{v}_1$ and $d\mathbf{v}_2$, centred at \mathbf{v}_1 and \mathbf{v}_2 , with their line of centres within the solid angle $d\mathbf{k}$ centred on \mathbf{k} , and with particle 1 located in the small volume $d\mathbf{x}$ centred on \mathbf{x} , is

$$4 f^{(2)}(\mathbf{v}_1, \mathbf{x}, \mathbf{v}_2, \mathbf{x} + 2a\mathbf{k}, t) a^2 (\mathbf{g} \cdot \mathbf{k}) d\mathbf{k} d\mathbf{v}_1 d\mathbf{v}_2 d\mathbf{x}. \quad (24)$$

Into this expression we may substitute Eq. (23) when we are ready.

2.2.3 The collisional production integral

The collisional rate of change per unit volume of some particle property ψ is the integral (taken over all possible binary collisions) of the change in ψ in a particular collision, multiplied by the probable frequency of such a collision. A factor of one half should also be included, otherwise we will count every collision twice (once for particle 1 and once for particle 2). We denote the resulting quantity by $C(\psi)$ and express it as

$$C(\psi) = 2 \int H(\mathbf{g} \cdot \mathbf{k}) \Delta(\psi) f^{(2)}(\mathbf{v}_1, \mathbf{x}, \mathbf{v}_2, \mathbf{x} + 2a\mathbf{k}, t) a^2 (\mathbf{g} \cdot \mathbf{k}) d\mathbf{k} d\mathbf{v}_1 d\mathbf{v}_2, \quad (25)$$

where the velocity integrations are over all space, the \mathbf{k} integrations are over the surface of the unit sphere, and H is the Heaviside step function (Jenkins and Richman, 1985). The step function ensures that the integration only includes real collisions, i.e. ones that satisfy $\mathbf{g} \cdot \mathbf{k} > 0$. Note importantly that $C(\psi)$ is nonlocal in space, because production of ψ at \mathbf{x} necessarily depends on the values that certain fields take at small but finite distances away. To determine the collisional production of second moment, $\psi = \mathbf{w}\mathbf{w}$, we use the expression (21) for $\Delta(\mathbf{w}\mathbf{w})$. We subsequently define $\mathbf{q} \equiv C(\mathbf{w}\mathbf{w})$ (cf. Eq. (14)).

If the system is dilute we set $FF \ll 1$ which forces $Y \approx 1$. Also we do not distinguish between the centres of the two particles, i.e. we assume the mean flow and the distribution function do not vary significantly on length scales of order a . Thus $\mathbf{h} \approx 0$ and $f(\mathbf{v}, \mathbf{x} + 2a\mathbf{k}, t) \approx f(\mathbf{v}, \mathbf{x}, t)$. If we set $\psi = \mathbf{w}\mathbf{w}$, these simplifications reduce expression (25) to that of Eq. (24) in Goldreich and Tremaine (1978).

2.2.4 The collisional flux of momentum

Consider the momentum transferred in a collision from particle 1 to particle 2 when they both straddle a surface of area dS with normal \mathbf{n} . The normal component of momentum transferred across the surface from particle 1 to particle 2 is then $m\mathbf{j} \cdot \mathbf{n}$, and the condition that the particles straddle the surface in the right sense is $\mathbf{k} \cdot \mathbf{n} > 0$.

Consider all the momentum transferred across the surface by such collisions.

Particle 2 must lie just above the surface and sit in a skew cylinder of volume $a(\mathbf{k} \cdot \mathbf{n})dS$. But the particle striking it must lie in the cylinder $4a^2(\mathbf{g} \cdot \mathbf{k})d\mathbf{k}dt$ (for collisions within solid angle $d\mathbf{k}$ and during time dt). Therefore, the average collision rate for particles with velocity ranges $d\mathbf{v}_1$ and $d\mathbf{v}_2$, straddling the surface dS , oriented in the range $d\mathbf{k}$ with particle 1 at \mathbf{x} is

$$4f^{(2)}(\mathbf{v}_1, \mathbf{x}, \mathbf{v}_2, \mathbf{x} + 2a\mathbf{k}, t)a^3(\mathbf{k} \cdot \mathbf{n})(\mathbf{g} \cdot \mathbf{k})d\mathbf{k}d\mathbf{v}_1d\mathbf{v}_2dS, \quad (26)$$

provided $\mathbf{g} \cdot \mathbf{k} > 0$ and $\mathbf{k} \cdot \mathbf{n} > 0$. The total momentum flux density resulting from collisions we denote by \mathbf{p}^c and define through

$$\mathbf{n} \cdot \mathbf{p}^c \equiv 4m a^3 \int H(\mathbf{g} \cdot \mathbf{k})f^{(2)}(\mathbf{v}_1, \mathbf{x}, \mathbf{v}_2, \mathbf{x} + 2a\mathbf{k}, t)(\mathbf{k} \cdot \mathbf{n})(\mathbf{g} \cdot \mathbf{k})\mathbf{j}d\mathbf{k}d\mathbf{v}_1d\mathbf{v}_2,$$

thus

$$\mathbf{p}^c = 2m a^3 \int H(\mathbf{g} \cdot \mathbf{k})f^{(2)}(\mathbf{v}_1, \mathbf{x}, \mathbf{v}_2, \mathbf{x} + 2a\mathbf{k}, t)(\mathbf{g} \cdot \mathbf{k})^2(1+\varepsilon)\mathbf{k}d\mathbf{k}d\mathbf{v}_1d\mathbf{v}_2. \quad (27)$$

If we assume that the mean flow \mathbf{u} varies slowly across a particle diameter, then we may write

$$\mathbf{h} = \mathbf{u}(\mathbf{x}, t) - \mathbf{u}(\mathbf{x} + 2a\mathbf{k}, t) \approx -2a\mathbf{k} \cdot \nabla \mathbf{u},$$

in which case we have the integral equivalent of Eq. (22):

$$\frac{1}{2}m \text{tr}(\mathbf{q}) = -D - \mathbf{p}^c : \nabla \mathbf{u} \quad (28)$$

where the rate of dissipation is

$$D = \frac{1}{2}a^2 m \int H(\mathbf{g} \cdot \mathbf{k})f^{(2)}(\mathbf{v}_1, \mathbf{x}, \mathbf{v}_2, \mathbf{x} + 2a\mathbf{k}, t)(1 - \varepsilon^2)(\mathbf{g} \cdot \mathbf{k})^3d\mathbf{k}d\mathbf{v}_1d\mathbf{v}_2. \quad (29)$$

This relates the collisional production of energy to the collisional momentum flux, and shows that the formalism is consistent; the quantity $\mathbf{p}^c : \nabla \mathbf{u}$ is just the rate at which the collisional momentum flux extracts energy from the mean flow.

2.2.5 The peculiar velocity distribution function

To make any progress in analysing the governing equations the integral expressions must be simplified. To that end we propose a specific model for the distribution function. First we introduce the peculiar velocity distribution function $f_{\mathbf{w}}(\mathbf{w}, \mathbf{x}, t)$ defined so that

$$f(\mathbf{v}, \mathbf{x}, t) = n(\mathbf{x}, t)f_{\mathbf{w}}(\mathbf{v} - \mathbf{u}(\mathbf{x}, t), \mathbf{x}, t).$$

Following Goldreich and Tremaine (1978) and AT86, a triaxial Gaussian model for $f_{\mathbf{w}}(\mathbf{w}, \mathbf{x}, t)$ is adopted:

$$f_{\mathbf{w}} = [(2\pi)^3 \det(\mathbf{W})]^{-1/2} \exp \left[-\frac{1}{2} \mathbf{W}^{-1} : \mathbf{w} \mathbf{w} \right], \quad (30)$$

where the dependence of $f_{\mathbf{w}}$ and \mathbf{W} on \mathbf{x} and t is understood. This form satisfies the required moment properties of Eqs (5)-(7).

To facilitate the manipulations of the next section we now assume \mathbf{W} does not vary appreciably on lengthscales of order a . This is acceptable if we only wish to analyse variations on long radial scales. In fact, if $a \sim H$ then the assumption is consistent with the closure scheme in Section 2.1. Note that we have already assumed vertical isothermality, and so \mathbf{W} 's variation with z is neglected.

2.2.6 Transformation of the integrals

First we transform from the variables $(\mathbf{v}_1, \mathbf{v}_2)$ to the relative and centre of mass velocities, $(\mathbf{g}, \mathbf{v}_c)$, the latter defined by

$$\mathbf{v}_c = \frac{1}{2}(\mathbf{w}_1 + \mathbf{w}_2).$$

The Jacobian determinant of the transformation is unity and the only appearance of \mathbf{v}_c in the integrands is in

$$f_{\mathbf{w}}(\mathbf{w}_1) f_{\mathbf{w}}(\mathbf{w}_2) = [(2\pi)^3 \det(\mathbf{W})]^{-1} \exp \left[-\mathbf{W}^{-1} : \left(\mathbf{v}_c \mathbf{v}_c + \frac{1}{4}(\mathbf{g} - \mathbf{h})(\mathbf{g} - \mathbf{h}) \right) \right].$$

This allows us to integrate over \mathbf{v}_c :

$$\int \exp \left[-\mathbf{W}^{-1} : \mathbf{v}_c \mathbf{v}_c \right] d\mathbf{v}_c = [\pi^3 \det(\mathbf{W})]^{1/2}.$$

What remains is

$$\mathbf{q} = 2a^2 \int H(\mathbf{g} \cdot \mathbf{k})(\mathbf{g} \cdot \mathbf{k}) \tilde{Y}(\mathbf{x}, \mathbf{k}) \Delta(\mathbf{w} \mathbf{w}) f_{\mathbf{g}}(\mathbf{g} - \mathbf{h}) d\mathbf{k} d\mathbf{g}, \quad (31)$$

$$\mathbf{p}^c = 2a^3 m \int H(\mathbf{g} \cdot \mathbf{k})(\mathbf{g} \cdot \mathbf{k})^2 \tilde{Y}(\mathbf{x}, \mathbf{k}) (1 + \varepsilon) f_{\mathbf{g}}(\mathbf{g} - \mathbf{h}) \mathbf{k} \mathbf{k} d\mathbf{k} d\mathbf{g}, \quad (32)$$

where we have introduced, for notational brevity, the function

$$\tilde{Y}(\mathbf{x}, \mathbf{k}) = Y[n(\mathbf{x} + a\mathbf{k})] n(\mathbf{x}) n(\mathbf{x} + 2a\mathbf{k}), \quad (33)$$

and a distribution function for \mathbf{g} ,

$$f_{\mathbf{g}}(\mathbf{g}) = [(4\pi)^3 \det(\mathbf{W})]^{-1/2} \exp \left(-\frac{1}{4} \mathbf{W}^{-1} : \mathbf{g} \mathbf{g} \right).$$

The latter is normalised such that $\int f_{\mathbf{g}} d\mathbf{g} = 1$. Note that $f_{\mathbf{g}}(\mathbf{g} - \mathbf{h})$ is an off-centred triaxial Gaussian, and the offset \mathbf{h} which derives from the background mean flow, will depend on \mathbf{k} .

We now tackle the \mathbf{g} integrals. We express \mathbf{g} space in Cartesian coordinates (X, Y, Z) , orienting them so $\mathbf{e}_Z = \mathbf{k}$. Thence we can remove the step function and replace the integration domain with the half space, $\{(g_X, g_Y, g_Z) : g_X, g_Y \in \mathbb{R}, g_Z \in \mathbb{R}^+\}$. This choice also simplifies the functional dependence of the coefficient of restitution to $\varepsilon = \varepsilon(g_Z)$. Consequently, the g_X and g_Y integrations are straightforward, and the g_Z integrations go through if we introduce certain ‘averages’ of ε . The biggest problem is returning the result to coordinate-free form, which requires some algebraic insight. But once this is done we have

$$\mathbf{q} = 2\pi^{-1/2}a^2 \int \tilde{Y} \zeta^{1/2} \times \left\{ \zeta \langle (1 + \varepsilon)^2 \rangle_3 F_1 \mathbf{K} - [(1 + \langle \varepsilon \rangle_3) F_1 - \xi(1 + \langle \varepsilon \rangle_2) F_2] \mathbf{G} \right\} d\mathbf{k}, \quad (34)$$

$$\mathbf{p}^c = 2\pi^{-1/2}a^3 \int \tilde{Y} \zeta (1 + \langle \varepsilon \rangle_2) F_2 \mathbf{K} d\mathbf{k}, \quad (35)$$

where the dyadics \mathbf{K} and \mathbf{G} are defined through

$$\mathbf{K} = \mathbf{k}\mathbf{k}, \quad \mathbf{G} = (\mathbf{W}\mathbf{k})\mathbf{k} + \mathbf{k}(\mathbf{W}\mathbf{k}), \quad (36)$$

the F functions are

$$F_1 = 2(1 + \xi^2)e^{-\xi^2} + \pi^{1/2}\xi(3 + 2\xi^2)(1 + \operatorname{erf} \xi), \quad (37)$$

$$F_2 = 2\xi e^{-\xi^2} + \pi^{1/2}(1 + 2\xi^2)(1 + \operatorname{erf} \xi), \quad (38)$$

where erf is the error function; the two variables ζ and ξ are defined through

$$\zeta = \mathbf{W} : \mathbf{k}\mathbf{k}, \quad \xi = \frac{1}{2} \frac{\mathbf{h} \cdot \mathbf{k}}{(\mathbf{W} : \mathbf{k}\mathbf{k})^{1/2}}, \quad (39)$$

and the average $\langle \psi \rangle_p$ by

$$\langle \psi \rangle_p(\zeta, \xi) = \frac{\int_0^\infty x^p \psi(x \zeta^{1/2}) e^{-x^2/4 + \xi x} dx}{\int_0^\infty x^p e^{-x^2/4 + \xi x} dx}, \quad (40)$$

for some general function $\psi(x)$. If ψ is a constant then $\langle \psi \rangle_p = \psi$. Expressions (34) and (35) are analogous to Araki and Tremaine’s (1986) but are more general as they include the dependence of ε on impact velocity. They are simpler, requiring the evaluation of two-dimensional rather than four-dimensional integrals, and also benefit from being coordinate free.

The quantities that appear in Eq. (39) have straightforward interpretations: ζ quantifies the magnitude of the squared impact velocity for a given orientation

\mathbf{k} , while ξ measures the ratio of the shear velocity across a particle radius to the velocity dispersion, and is hence $\propto R$. This means dilute expressions may be recovered by letting $\xi = 0$ and $\tilde{Y} = n(\mathbf{x})^2$.

In order to evaluate the remaining integrals, expressions for ε and \mathbf{h} must be supplied. The experimentally derived, piecewise power law of (1) is the obvious choice for ε , while we treat the velocity gradient as locally uniform, as before, i.e. $\mathbf{h} = -2a \mathbf{k} \cdot \nabla \mathbf{u}$. Therefore:

$$\xi = -a \frac{(\mathbf{e} : \mathbf{k}\mathbf{k})}{(\mathbf{W} : \mathbf{k}\mathbf{k})^{1/2}}$$

where \mathbf{e} is the rate of strain tensor.

In addition, we require the form of $n(\mathbf{x})$ and $Y[n(\mathbf{x})]$. The Enskog factor may take one of the formulae mentioned, but the number density should be determined from the vertical momentum balance. Alternatively, an explicit form could be supplied. We discuss these issues a little later.

The integral terms as they stand, though still involved can be computed numerically without much difficulty. Nonetheless, additional assumptions yield further useful simplifications.

First, we may suppose that n does not vary appreciably on scales of order a ; so, like \mathbf{W} , it may be considered to be the same at the position of each particle in contact: i.e. $\mathbf{x}_1 = \mathbf{x}_2 = \mathbf{x}$. Then

$$\tilde{Y} = Y[n(\mathbf{x})] n(\mathbf{x})^2 \quad (41)$$

and can be brought outside the integral. This means that as far as the collision frequency is concerned nonlocality is neglected and n is constant; for all other purposes (in the height equation, etc) n varies and must be determined from (19). If we consider homogeneous equilibria or largescale horizontal variations, n will only exhibit appreciable variations in the z direction (the disk thickness being of order a) and so, essentially, it is this vertical variation that \tilde{Y} omits. We hence refer to the adoption of (41) as ‘vertical locality’, as opposed to the ‘vertical nonlocality’ of the full model (Eq. (33)). Note that nonlocality in the shear, introduced by \mathbf{h} , remains and is crucial.

Second, we may suppose that for the purposes of the collisional kinematics the coefficient of restitution is an averaged quantity dependent on only macroscopic variables, principally c , as was done in Latter and Ogilvie (2006). Hence, ε is constant as far as the integrations are concerned.

Third, we may approximate the integrands by polynomial interpolation or series expansion. These approaches are valid if dense effects and/or anisotropy is

small, and permit the remaining integrations to go through. We shall examine the last two assumptions in some detail.

2.2.7 Averaging the coefficient of restitution

As we have seen, the expressions for \mathbf{q} and \mathbf{p}^c involve various averages of ε which are described in Eq. (40). These can only be analytically evaluated for relatively simple functions, and then the result is rather complicated. For example, if we set the coefficient to be a straight power law, $\varepsilon = (\mathbf{g} \cdot \mathbf{k}/v_c)^{-p}$, we get

$$\langle \varepsilon \rangle_2 = \frac{2^{4-2p}}{\sqrt{\pi}} \Gamma(2 - \tfrac{1}{2}p) \Gamma(\tfrac{3}{2} - \tfrac{1}{2}p) \left(\frac{\sqrt{\zeta}}{v_c} \right)^{-p} \cdot \left(\frac{e^{-\xi^2}}{F_2(\xi)} \right) H_{p-3}(-\xi), \quad (42)$$

$$\langle \varepsilon \rangle_3 = \frac{2^{5-2p}}{\sqrt{\pi}} \Gamma(\tfrac{5}{2} - \tfrac{1}{2}p) \Gamma(2 - \tfrac{1}{2}p) \left(\frac{\sqrt{\zeta}}{v_c} \right)^{-p} \cdot \left(\frac{e^{-\xi^2}}{F_1(\xi)} \right) H_{p-4}(-\xi), \quad (43)$$

where H_ν is the Hermite function, Γ is the gamma function (Abramowitz and Stegun, 1965), and F_1 and F_2 are given by Eqs (37) and (38). Unfortunately, more complicated functions, including the more accurate piecewise law, do not yield a closed form for $\langle \varepsilon \rangle_q$, in which case the collision terms require the numerical evaluation of three integrals each.

We aim to employ the piecewise ε law and, given that the collision terms are sufficiently complicated, it would be convenient if we could eliminate the third integral. Moreover, expressions like (42) and (43) are complicated functions of the integration variable \mathbf{k} and hence computationally more intensive. These considerations motivate the technique of ‘preaveraging’. Because the elasticity laws we possess are in some sense ‘the average’ of a number of experimental collisions anyway, philosophically, at least, this approximation is justified. In this subsection we provide details of a possible preaveraging process.

Let us define $A_\gamma(\psi)$ as the weighted average of the function $\psi(\mathbf{g} \cdot \mathbf{k})$ over all collisions. The weighting function is $(\mathbf{g} \cdot \mathbf{k})^{\gamma-1}$, and γ is a real positive number. We define

$$A_\gamma(\psi) \equiv \frac{\int H(\mathbf{g} \cdot \mathbf{k}) \psi(\mathbf{g} \cdot \mathbf{k}) Y f_1 f_2 (\mathbf{g} \cdot \mathbf{k})^\gamma d^2 \mathbf{k} d^3 \mathbf{w}_1 d^3 \mathbf{w}_2}{\int H(\mathbf{g} \cdot \mathbf{k}) Y f_1 f_2 (\mathbf{g} \cdot \mathbf{k})^\gamma d^2 \mathbf{k} d^3 \mathbf{w}_1 d^3 \mathbf{w}_2} \quad (44)$$

where f_1 and f_2 represent the peculiar velocity distribution function evaluated at particle 1 and 2 respectively. Obviously, $A_\gamma(\psi) = \psi$ if ψ is a constant. We now replace each instance of $\langle \varepsilon \rangle_q$ with $A_q(\varepsilon)$, i.e. $\langle \varepsilon \rangle_q \approx A_q(\varepsilon)$. For a simpler but less accurate formalism, we replace every instance of $\langle \varepsilon \rangle_q$ with $A_\gamma(\varepsilon)$ for a *fixed* γ for all q .

The integral (44) can be evaluated by the same techniques as earlier if it

is assumed that f is a triaxial Gaussian. However, the result is relatively complicated and it so happens there is little gain over the fully consistent model of (34) and (35). An acceptable approximation is the adoption in (44) of a Maxwellian, $f \propto \exp[-w^2/(2c^2)]$. However to complete all the integrals we must adopt (41) and neglect the nonlocal contributions, i.e. set $\xi = 0$. This is less justifiable but mathematically advantageous and, in fact, yields results in good agreement with the full model, as we explore in Section 3.10.

Implementing these approximations for the piecewise power law function, $\varepsilon = \min\{1, (\mathbf{g} \cdot \mathbf{k}/v_c)^{-p}\}$, yields

$$A_2(\varepsilon) = \operatorname{erf} X - \frac{2}{\sqrt{\pi}} X \left(1 + \frac{1}{\mu_2} X^2\right) e^{-X^2} - \frac{2}{\mu_2 \sqrt{\pi}} X^5 E_{\mu_2}(X^2) \quad (45)$$

$$A_3(\varepsilon) = 1 - \left(1 + X^2 - \frac{2}{\mu_3} X^4\right) e^{-X^2} - \frac{1}{2\mu_3} X^6 E_{\mu_3}(X^2) \quad (46)$$

where $X = v_c/(2c)$, $\mu_s = (p - 1 - s)/2$, and $E_\mu(x)$ is the exponential integral E function. Though they may seem a little complicated, these expressions are especially helpful because they involve only the squared velocity dispersion (c^2) and none of the integration variables (through ζ and ξ). Consequently, they can be brought out of the integrals entirely.

2.2.8 Interpolating the integrands

Because the F functions rapidly increase with ξ , their Taylor series (truncated at a manageable order) are poor approximations unless ξ is very small. But dense ring equilibria fall into the regime of $|\xi| \sim 1$. An alternative is to interpolate the f 's on some range of ξ , which we can estimate from Eq. (39).

To proceed, vertical locality is assumed, so that $\tilde{Y} = Y(\mathbf{x}) n^2(\mathbf{x})$, and ε is treated as preaveraged, with the additional approximation, $A_2(\varepsilon) = A_3(\varepsilon)$ in the collisional production integral. Enforcing these gives

$$\begin{aligned} \mathbf{q} &= 2\pi^{-1/2} a^2 \tilde{Y} [1 + A_3(\varepsilon)] \left\{ [1 + A_3(\varepsilon)] \int \zeta^{3/2} F_1 \mathbf{K} d\mathbf{k} - \int \zeta^{1/2} F_3 \mathbf{G} d\mathbf{k} \right\}, \\ \mathbf{p}^c &= 2\pi^{-1/2} a^3 \tilde{Y} [1 + A_2(\varepsilon)] \int \zeta F_2 \mathbf{K} d\mathbf{k}, \end{aligned}$$

where $F_3 \equiv F_1 - \xi F_2$.

We now interpolate the F functions. For small anisotropy we have the upper bound

$$|\xi| < \frac{3}{2} R \left\| \frac{\mathbf{e}}{\Omega} \right\|,$$

which for equilibrium solutions with $R < 1$ gives $|\xi| < 9/8$. On this range we find that F_1 can be successfully interpolated by a cubic in ξ , and F_2 and F_3

by quadratics:

$$F_1 = \sum_{n=0}^3 F_{1n} \xi^n, \quad F_2 = \sum_{n=0}^2 F_{2n} \xi^n, \quad F_3 = \sum_{n=0}^2 F_{3n} \xi^n. \quad (47)$$

where the F_{jn} are pure numbers arising from the interpolation range and the interpolation method.

Next, we express

$$\mathbf{W} = c^2(\mathbf{1} + \mathbf{a})$$

where the squared velocity dispersion is $c^2 = \text{Tr}(\mathbf{W})/3$ and \mathbf{a} is the anisotropy tensor, which is symmetric and traceless. It follows that

$$\boldsymbol{\pi} = -mn c^2 \mathbf{a}$$

if the viscous stress is denoted by $\boldsymbol{\pi}$. Because $\|\mathbf{a}\| < 1$, the integrands may be systematically expanded in \mathbf{a} through

$$\xi = -\frac{a}{c} (\mathbf{e} : \mathbf{k}\mathbf{k}) \left[1 - \frac{1}{2} \mathbf{a} : \mathbf{k}\mathbf{k} + \frac{3}{4} (\mathbf{a} : \mathbf{k}\mathbf{k})^2 + \mathcal{O}(\mathbf{a}^3) \right],$$

and

$$\zeta = c^2 [1 + \mathbf{a} : \mathbf{k}\mathbf{k}].$$

Now we are in a position to evaluate the integrals directly. Expressions for \mathbf{q} and \mathbf{p}^c may be written in terms of spherical surface integrals of the form

$$J_{i_1 i_2 \dots i_{2l}} = \frac{1}{4\pi} \int_S k_{i_1} k_{i_2} \dots k_{i_{2l}} d\mathbf{k},$$

where S is (the surface of) the unit sphere. Necessarily

$$J_{i_1 i_2 \dots i_{2l}} = \frac{1}{2l+1} I_{i_1 i_2 \dots i_{2l}},$$

where

$$I_{i_1 i_2 \dots i_{2l}} = \delta_{(i_1 i_2} \delta_{i_3 i_4} \dots \delta_{i_{2l-1} i_{2l}}),$$

and is the unique, totally symmetric, isotropic tensor of rank $2l$. Parantheses around a set of j indices denote the sum of all permutations of the indices divided by $j!$

The closed forms of the integrands to $\mathcal{O}(\mathbf{a})$ are presented in Appendix A, and, though complicated, are algebraic functions. As such, they possess a great numerical advantage over previous kinetic approaches, and certainly pave the way for dynamical analyses, particularly nonlinear studies, which have been the sole preserve of hydrodynamics.

The main errors that characterise this formalism arise from truncation in \mathbf{a} . Thus, significantly anisotropic systems may not be well described (for instance,

rings suffering very few collisions). In addition, when the velocity dispersion is extremely low or the rate of strain large, the interpolation range must be extended, and at some point the interpolating polynomials may be of too low an order to adequately approximate F_1 , F_2 , and F_3 . This should only be an issue for some nonlinear calculations, however.

2.2.9 Expanding the integrands

We have argued that a real ring lies in the regime $\xi \sim 1$, but it is nevertheless interesting to examine ‘warm’ and dilute rings for which ξ is small. Doing so allows us to connect our formalism to other well-known kinetic models, such as those of Goldreich and Tremaine (1978), and Jenkins and Richman (1985).

We expand the integrands of \mathbf{q} and \mathbf{p}^c first in powers of ξ and then in \mathbf{a} , assuming both are small. All the integrals then can be performed much as before. In the interest of space we omit these details.

The closed algebraic expressions for \mathbf{q} and \mathbf{p}^c so obtained are analogous to, and possibly more systematic than, those computed by Jenkins and Richman (1985), who employ Grad’s prescription for the single particle distribution function (Grad, 1949). They concentrate on the case when the spatial derivatives of the mean fields are small, and the distribution nearly isotropic. In the language of our model, they examine orders up to and including (ξ^0, \mathbf{a}^1) and (ξ^1, \mathbf{a}^0) , and then in the hydrodynamic limit, ω_c large. This permits them to obtain constitutive expressions for the hydrodynamic transport coefficients — shear and bulk viscosities and thermal conductivity. Interestingly we can recover precisely the same expressions, despite the difference in our choice of distribution function.

The leading terms, of order ξ^0 , are just the collision integrals for a dilute gas. And because of the triaxial Gaussian ansatz adopted they coincide with the collision term of the Goldreich and Tremaine (1978) model up to whichever order in \mathbf{a} we choose to truncate. After vertical averaging we obtain

$$\mathbf{Q} = \frac{8}{\pi} \tau \Omega N c^2 (1 + \varepsilon) \left[-\frac{1}{3}(1 - \varepsilon) \mathbf{1} - \frac{1}{5}(3 - \varepsilon) \mathbf{a} + \mathcal{O}(\mathbf{a}^2) \right].$$

In contrast, the model of Shu and Stewart (1985) gives

$$\mathbf{Q} = \frac{8}{\pi} \tau \Omega N c^2 (1 + \varepsilon) \left[-\frac{1}{3}(1 - \varepsilon) \mathbf{1} - \left(\frac{1}{1 + \varepsilon} \right) \mathbf{a} \right],$$

and their interpretation of the ‘dilute’ Hämeen-Anttila model (Hämeen-Anttila, 1978, 1981) is

$$\mathbf{Q} = \frac{8}{\pi} \tau \Omega N c^2 (1 + \varepsilon) \left[-\frac{1}{3}(1 - \varepsilon) \mathbf{1} - \frac{1}{6}(3 - \varepsilon) \mathbf{a} \right].$$

Here upper case indicates vertical averaging, as before. All these models agree at $\mathcal{O}(\mathbf{a}^0)$ but disagree at $\mathcal{O}(\mathbf{a})$. However, the difference at this order between the Goldreich and Tremaine and Hämeen-Anttila models is only a small difference in the constant coefficient (1/6 against 1/5). This accounts for the (relatively) good agreement these two models enjoy in equilibrium calculations (Stewart *et al.*, 1984).

3 Equilibria

Now that the various models have been sketched, we employ them to calculate dense ring equilibria. We solve for the vertically averaged pressure tensor and the disk height for a given vertical structure of n . First, we compare the results predicted by our kinetic model with those produced by the kinetics of AT86 and the N -body simulations of Wisdom and Tremaine (1988) and Salo (1991). Second, we test the appropriateness of the three models introduced in the preceding sections, namely, that of ‘vertical locality’, the ‘preaveraged’ ε model, and the interpolation model. Because these formalisms significantly simplify the problem it is worthwhile testing the approximations upon which they are founded.

3.1 Governing equations

We calculate the steady homogeneous state of a disk rotating about a perfectly spherical planet and whose self-gravity is negligible in the horizontal balances. In the shearing sheet this equates to $n = n_0(z)$ and $\mathbf{u} = -(3/2)\Omega x \mathbf{e}_y$. The equilibrium pressure tensor equations are

$$4\Omega W_{xy} + Q_{xx}/N = 0, \quad (48)$$

$$-\frac{1}{2}\Omega W_{xx} + 2\Omega W_{yy} + Q_{xy}/N = 0, \quad (49)$$

$$-\Omega W_{xy} + Q_{yy}/N = 0, \quad (50)$$

$$Q_{zz} = 0, \quad (51)$$

where, as earlier, upper case indicates vertical averaging (except in the case of W_{ij} and c which we assume independent of z). The natural nondimensionalisation of this system is founded on particle radius and orbital frequency, so that

$$t = \Omega^{-1}t^*, \quad x = ax^*, \quad \mathbf{u} = a\Omega\mathbf{u}^*, \quad W_{ij} = a^2\Omega^2 W_{ij}^*,$$

where asterisked quantities are dimensionless.

In addition to this set of equations we need expressions for $n_0(z)$, $Y[n]$ and ε .

The last two can be supplied by simulations or experiments. The first can be determined from the vertical hydrostatic balance (19). We visit each in turn.

3.2 The Enskog factor

The Enskog factor is modelled according to Araki and Tremaine’s prescription: a polynomial fit to the molecular dynamics data of Alder and Wainwright (in Ree and Hoover, 1967)²:

$$Y(\text{FF}) = \sum_{i=0}^5 D_i \text{FF}^i \quad (52)$$

where

$$\begin{aligned} D_0 &= 1.0000, & D_1 &= 3.5496, & D_2 &= -18.816 \\ D_3 &= 165.30, & D_4 &= -407.27, & D_5 &= 406.94 \end{aligned}$$

Though strictly applicable to only non-shearing gases of elastic spheres, this prescription should capture the qualitative behaviour of the Enskog factor in an inelastic system (see AT86).

3.3 The coefficient of restitution

For ε we mainly use the piecewise power law of (1) which has been experimentally derived by Bridges *et al.* (1984), Hatzes *et al.* (1988), and Supulver *et al.* (1995) for sufficiently frosted ice particles in Saturnian conditions. The two parameters p and v_c we let vary, though recognising that Bridges’ data give their values as 0.234 and 0.0077 cm s^{−1}, Hatzes’ data 0.20 and 0.025 cm s^{−1}, and Supulver’s 0.19 and 0.029 cm s^{−1}. The preaveraged ε ’s take the functional form of (45) and (46) in the collision terms. For one calculation we employ the power law form of ε , for which we use the fully consistent expressions (42) and (43). These forms introduce the important dimensionless quantity $R_c \equiv a\Omega/v_c$ which controls to some extent the equilibrium velocity dispersion of the particles.

² It should be noted that the values given by Araki & Tremaine (1986) contain a typographical error. Their coefficient D_3 must read 0.8874 not 0.08874 (Juergen Schmidt, private communication).

3.4 The height equation and vertical locality

Instead of solving for n a convenient alternative is to assume it takes a specific form (AT86), either a Gaussian or polytrope. In this case Eq. (19) becomes an algebraic equation for H . This is then solved with the set (48)–(51).

In the case of Gaussian vertical structure, we write,

$$n_0(z) = \tilde{n} \exp \left[-\frac{z^2}{2H^2} \right], \quad (53)$$

where H is the disk scale height and \tilde{n} a constant. Consequently we can determine the optical depth from

$$\tau = \frac{3\sqrt{2\pi}}{4} \frac{H}{a} \text{FF}_0, \quad (54)$$

where $\text{FF}_0 = \text{FF}[\tilde{n}]$, i.e. the filling factor in the midplane ($z = 0$). This expression gives flesh to the estimate (4).

After multiplication by z and vertical integration, the hydrostatic balance (19) becomes

$$\Omega^2 H^2 \left[1 + \frac{3}{2} \sqrt{2} G_s \text{FF}_0 \right] - W_{zz} - P_{zz}/N = 0, \quad (55)$$

where $N = \sqrt{2\pi} H \tilde{n}$ is the surface number density and

$$G_s \equiv \frac{G m}{\Omega^2 a^3} = \left(\frac{\rho_p}{\rho_S} \right) \left(\frac{r}{r_S} \right)^3,$$

expresses the disk self-gravity. Here ρ_p and ρ_S are the internal mass densities of a particle and the planet respectively, r is distance from the centre of the planet, and r_S is the radius of the planet itself. In Saturn's case, $\rho_S = 618 \text{ kg m}^{-3}$ and $r_S = 6.03 \times 10^4 \text{ km}$; we then have

$$G_s = 0.735 \times \left(\frac{r}{10^5 \text{ km}} \right)^3 \left(\frac{\rho_p}{100 \text{ kg m}^{-3}} \right). \quad (56)$$

For particles composed of solid ice, $\rho_p = 900 \text{ kg m}^{-3}$, the parameter G_s varies from about 6 at the inner edge of the B-ring, to 7.7 at the outer edge of the B-ring, to approximately 9 at the outer edge of the A-ring. Of course, these estimates are rather rough. The internal density of real ring particles may depart significantly from that of solid ice: particles may, for instance, be far more ‘fluffy’ and possess a density less than that quoted (see, for example, Weidenschilling *et al.*, 1984).

A polytropic model can be described by

$$n_0(z) = \tilde{n} \left(1 - \frac{z^2}{H^2} \right)^\alpha \quad (57)$$

for a given constant α . Then the optical depth is

$$\tau = \frac{3\sqrt{\pi}}{4} \frac{\Gamma(1+\alpha)}{\Gamma(3/2+\alpha)} \frac{H}{a} \text{FF}_0 \quad (58)$$

and the vertical hydrostatic balance differs little in form from (55) except for the addition of the new parameter α ,

$$\Omega_0^2 H^2 \left(\frac{1}{2}(\alpha + \frac{3}{2})^{-1} + \frac{3}{2} g(\alpha) G_s \text{FF}_0 \right) - W_{zz} - P_{zz}^c/N = 0, \quad (59)$$

where

$$g(\alpha) = \frac{2^{2\alpha+1}}{\sqrt{\pi}(\alpha+1)} \cdot \frac{\Gamma(\alpha + \frac{3}{2})^2}{\Gamma(2\alpha + \frac{5}{2})}.$$

This approximation has been used by Borderies, Goldreich and Tremaine (1985) and Mosquera (1996) (with $\alpha = 1$) and is more accurate than the Gaussian model at describing monodisperse disks at moderate and large filling factors, as we shall see. A problem, however, is the specification of α which may vary with FF_0 but which cannot be determined from the governing equations. That said, our equilibrium solutions show that the equilibrium quantities are relatively insensitive to the precise choice of α .

If we assume vertical locality, the scale height H can be removed from the viscous stress equations (48)–(51) completely. Moreover we can solve for H explicitly in (55) or (59) once the viscous stress components are known, because then \bar{Y}/N , and thus P_{zz}^c/N , is independent of H . In the case of the vertical Gaussian, the averaged Y is

$$\bar{Y}/N = \frac{3}{16\pi a^3} \left(\sum_{j=0}^5 D_j \text{FF}_0^{j+1} / \sqrt{j+2} \right). \quad (60)$$

In the case of the polytrope, we compute

$$\bar{Y}/N = \frac{3}{16\pi a^3} \left(\sum_{j=0}^5 D_j \text{FF}_0^{j+1} \frac{\Gamma(\alpha + 3/2) \cdot \Gamma(j\alpha + 1)}{\Gamma(\alpha + 1) \cdot \Gamma(j\alpha + 3/2)} \right). \quad (61)$$

If we do not adopt vertical locality then H appears in all the vertically averaged equilibrium equations through the vertically averaged \tilde{Y} (cf. Eqs (34) and (35)). The height equation must then be solved concurrently with (48)–(51). Unfortunately, the vertical integration can only be accomplished analytically for the Gaussian model. Usage of the polytrope model must be accompanied

by the assumption of vertical locality, unless we compute the extra integral numerically.

In the Gaussian case, vertical nonlocality engenders the additional factor $\exp[-(a^2/H^2)k_z^2]$ in (60). This ‘weighting function’ diminishes the effect of those collisions in which the particles inhabit different vertical strata, or, put another way, are oriented ‘more vertically’ with respect to each other (exhibiting larger k_z). It follows that the factor takes values between 1 (‘perfectly horizontal’ collisions) and $\exp[-a^2/H^2]$ (‘almost vertical’ collisions). When the disk is thick (meaning, a/H is small) then this range is very narrow and the factor is essentially 1; vertical nonlocality is then unimportant. In the extremely thin limit, i.e. $a/H \sim 1$, the factor can be smaller than e^{-1} , which expresses the simple fact that in a near monolayer it would be unusual to find a pair of particles inhabiting very different vertical positions.

Finally we present an expression for the collision frequency. This should scale roughly like $\pi a^2 c Y n$. After inspecting (24), we settle on

$$\omega_c = 16\pi^2 a^2 c \left(\overline{Y}/N \right), \quad (62)$$

in which the constant coefficient is chosen so that the expression conforms with the dilute ω_c calculated by Shu and Stewart (1985). In this limit the vertical structure is Gaussian and we obtain a simple linear dependence on optical depth: $\omega_c = (8/\pi)\Omega\tau$.

3.5 Numerical technique

The equilibrium solution requires the roots of the algebraic system (48)–(51); if vertical nonlocality is included we must add the the height equation (55) or (59) to this set. As these equations involve integral functions of W_{ij} a number of numerical techniques are needed. The solutions are obtained by using the multi-dimensional Newton’s method, while the spherical surface integrations are broken into azimuthal angle, which are accomplished using the trapezoidal rule, and meridional angle, which are accomplished using Gaussian quadrature. *Mathematica* was the programming language used, and the special functions that appear in the integrals are evaluated using the *Mathematica* routines. If ε is specified, as either a constant or a function of $\mathbf{g} \cdot \mathbf{k}$, the equilibrium solution W_{ij} (and H) depends only on the parameter FF_0 .

3.6 Comparison with the model of Araki and Tremaine (1986)

In order to check our model we compared its predictions with those of AT86, who adopt a constant ε , Gaussian vertical structure and vertical nonlocality. If we do the same, the two models should produce identical results because they share exactly the same assumptions.

We computed equilibrium properties with our formalism and checked it against those produced by the Araki and Tremaine model (Schmidt, private communication). The parameters used were $\varepsilon = 0$ and $G_s = 7.4$, on one hand, and $\varepsilon = 0.5$ and $G_s = 0$ on the other. Agreement to four significant figures was obtained and this seemed only limited to the accuracy chosen for the numerical integrations. These results prove that the formalism we develop in this paper is equivalent to that of AT86.

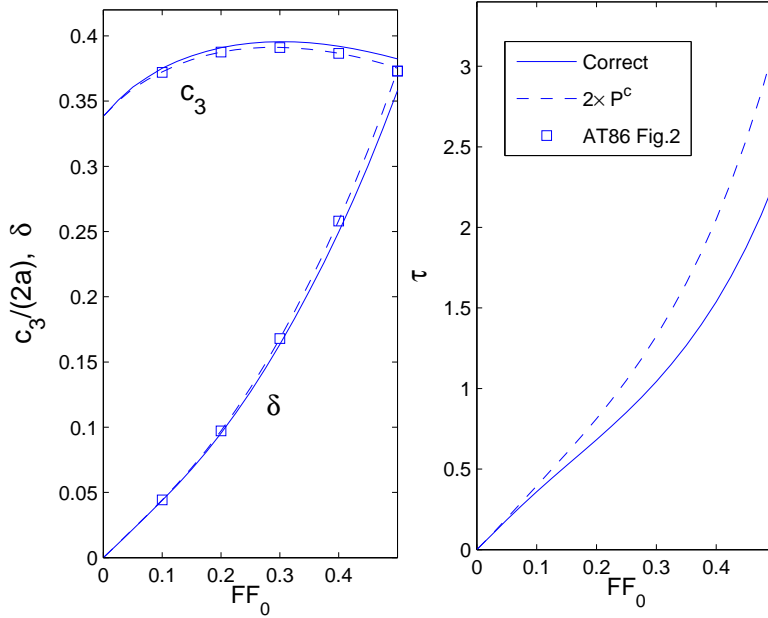


Fig. 1. In these figures we show the effect on certain equilibrium properties when a factor 2 is introduced into the collisional transport term, P_{zz}^c . Additionally, we plot points from Fig. 2 in AT86 in order to demonstrate that their computational routine suffers the factor 2 error. In subplot (a), we present the orientation angle of the velocity ellipsoid δ and the vertical velocity dispersion c_3 . The parameters taken are $\epsilon = 0$ and $G_s = 7.4$. In subplot (b), we present optical depth τ . The parameters are $\epsilon = 0.5$ and $G_s = 0$. Generally the discrepancy is small, except in τ and H when self-gravity is weak.

It should be mentioned that the kinetic equilibria in Araki and Tremaine (1986), and also Wisdom and Tremaine (1988), were computed by a routine which introduces an erroneous factor of two in the calculation of P_{zz}^c (given

by their Eq. (142)). As a consequence their computations overestimate the amount of collisional momentum transport in the vertical direction. In the self-gravitating case $G_s = 7.4$, which appears in AT86, the discrepancy is small but noticeable. We illustrate the discrepancy in Fig. 1a and also plot some points from Araki and Tremaine’s Fig. 2. As is clear, the latter sit perfectly on the calculation that doubled P_{zz}^c . In contrast, when self-gravity is omitted, the overestimated collisional flux has greater influence, but only on those quantities which depend closely on the vertical problem, namely optical depth τ and scale height H . This is demonstrated in Fig. 1b where we plot τ versus FF_0 for the case $\varepsilon = 0.5$ and $G_s = 0$. For large FF_0 the discrepancy can be as large as 35%.

3.7 Comparison with the simulations of Wisdom and Tremaine (1988)

The discrepancy just mentioned means that the agreement between the simulations of Wisdom and Tremaine (1988) and the AT86 kinetics with respect to τ no longer holds, cf. their Fig. 15. We stress, though, that the good agreement witnessed by the ‘horizontal’ equilibrium properties, (as functions of FF_0) remain.

The disagreement in τ we blame on the assumption of the Gaussian vertical profile, which is appropriate at low FF_0 but less so at higher filling factors, when the disk establishes a vertical structure akin to a polytrope (see Fig’s 3, 4, 8, and 9 in Wisdom and Tremaine, 1988). These two regimes and the transition between them can only be captured by a kinetic model that properly solves the vertical hydrostatic equilibrium, which is precisely what is done in Araki (1991). The agreement with Wisdom and Tremaine’s simulations in this work is excellent, though the kinetic theory is computationally expensive and suffers numerical difficulties.

As an alternative to the approach of Araki (1991), we apply a model in which polytropic vertical structure is assumed from the outset. Such a model should approximate well the middle to larger filling factor regimes and tolerably approximate the low filling factor regime, thus saving us the arduous task of computing the vertical hydrostatic balance exactly.

Subsequently, we computed equilibria using the polytropic formalism embodied in (57)-(59), and (61) using a fixed α and $\varepsilon = 0.5$ and $G_s = 0$. Much better agreement was obtained with the Wisdom and Tremaine simulations at middling and larger filling factors and reasonable agreement at lower filling factors (cf. Fig. 2). Indeed, Fig. 2a nicely illustrates the transition between the two regimes — Gaussian at lower FF_0 and polytropic at middle to large FF_0 . The transition occurs around $\text{FF}_0 = 0.275$ or about $\tau = 1$. Additionally, we plot

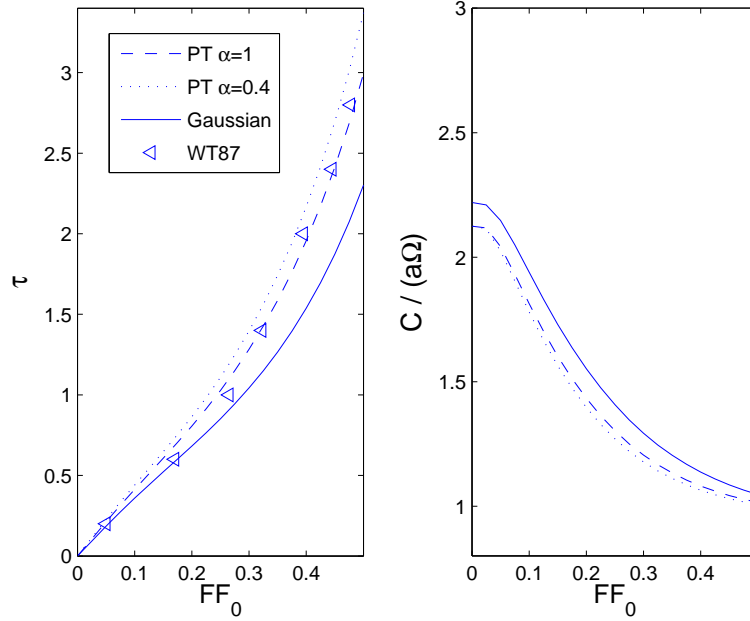


Fig. 2. (a) Here we plot optical depth τ , as a function of central filling factor FF_0 , computed by various methods. The dashed and dotted lines correspond to kinetic models with polytropic vertical structure (‘PT’) and $\alpha = 0.4$ and $\alpha = 1$ respectively. The solid line corresponds to a kinetic model with Gaussian vertical structure. The diamond points (WT88) correspond to the simulations of Wisdom and Tremaine (1988), read from their Fig. 15. (b) The second panel presents velocity dispersion C , as a function of central filling factor, computed by the three kinetic models. The coefficient of restitution is set to 0.5 and $G_s = 0$ in all cases.

the velocity dispersion versus FF_0 to show, in contrast, that the horizontal equilibrium properties are little altered by the choice of vertical model.

Fig. 2

The range of α that we employed was informed by simple inspection of the vertical profiles of Wisdom and Tremaine (1988). These indicated that α takes values between 1 to about 0.4 (and perhaps lower). It is clear, though, that changing α does not significantly alter the equilibrium properties, certainly not for W_{ij} , as can be seen in Fig. 2b. Thus it appears the polytropic model constrains the equilibrium behaviour to a separate regime effectively independent of the specific choice of α : this means we can’t just produce any result we like by tweaking α . However, the best agreement is obtained with $\alpha = 0.9$ and we employ that value throughout the rest of the paper.

3.8 Comparison with Salo (1991)

We next compare our equilibrium results with those of Salo’s (1991) simulations for which the coefficient of restitution varies as a function of impact velocity. This supplies us with results with which to test the kinetic model’s treatment of nonconstant ε . Moreover, this set of data is particularly useful as it includes a number of runs with different v_c , one of the key parameters in our model. The disk, otherwise, is non-self-gravitating, and particles are assumed to possess a radius of 100 cm and orbit at the location in the B-ring where $a\Omega = 0.02 \text{ cm s}^{-1}$. Collisions dissipate energy according to the piecewise power law, Eq. (1), with $p = 0.234$ and v_c a multiple of $v_b = 0.01 \text{ cm s}^{-1}$. By varying v_c the parameter R_c can be controlled, which roughly governs the velocity dispersion and the ‘denseness’ or ‘diluteness’ of the gas, at least for intermediate collision frequencies.

We will actually compare our results with more recent equilibrium simulations which reproduce the runs of Salo (1991) but with a five-fold increase in particle number and duration (Salo, private communication). The results are much the same but with reduced scatter.

The kinetic model adopted in this section employs

- a preaveraged ε , the piecewise power law, using (45) and (46)
- polytropic vertical structure with $\alpha = 0.9$
- vertical locality.

When nondimensionalised the model depends on p , $R_c = a\Omega/v_c$, G_s , and FF_0 . In this section $G_s = 0$ and $p = 0.234$ as mentioned, and FF_0 and $R_c = 2(v_b/v_c)$ will vary. Once supplied with these inputs our algorithm produces the nondimensionalised W_{ij} and then computes a number of related properties: the viscosities,

$$\nu^L = \frac{W_{xy}}{3\Omega/2}, \quad \nu^{NL} = \frac{P_{xy}^c/N}{3\Omega/2},$$

the disk semithickness H , optical depth τ , and preaveraged coefficient of restitution, $A_3(\varepsilon)$. Throughout this section the quantity $A_3(\varepsilon)$ will be referred to as simply ε .

3.8.1 Results

In Fig. 3 we plot the equilibrium velocity dispersion, the disk scale height, the averaged ε , and the central filling factor against τ for various v_c . In Fig. 3a we also include the results of Salo’s simulations.

As is clear from Fig. 3a the kinetics and the simulations are consistent, and

match particularly well when filling factor is high. In general, the kinetic model slightly overestimates the velocity dispersion, particularly at low optical depths. The preaveraging assumption probably contributes most heavily to this discrepancy. Errors arising from the assumptions of vertical locality should be secondary because the disk thickness H is relatively large (cf. Fig. 3c). But the choice of polytropic vertical structure may play some part, even though Fig. 2b suggests that a Gaussian model would also overestimate C . For large ratios v_c/v_b — when the velocity dispersion is large and FF_0 low (see Fig. 3d) — the vertical disk structure will probably resemble a Gaussian not a polytrope.

These considerations aside, the general trend is quite clear: as v_c increases so does the equilibrium velocity dispersion. This admits a relatively straightforward interpretation. Because collisions must dissipate energy to offset viscous heating, C must be at least $\mathcal{O}(v_c)$: if C were much less than v_c very little energy at all would be lost in collisions and certainly not enough to maintain an energy balance. It must follow that if v_c is increased so must the equilibrium C .

The magnitude of the velocity dispersion has a direct bearing on the thickness of the disk as Fig. 3b can attest. Here we can see how the particles' collisional properties closely constrain important features of the disk. For the more dilute disks, H is directly correlated with c and seems to adhere quite well to the dilute estimate of $H \approx c/\Omega$. In contrast, it behaves quite differently in the case of $v_c/v_b = 1$. Here H possesses a subtle turning point at a critical τ after which it begins to increase. The increase is caused by the vertical flux of momentum due to collisions, the 'collisional pressure', which increases with τ . As the translational pressure drops and the disk vertically contracts this contribution will become important and will work to fatten the disk. If we had included self-gravity, however, the collisional pressure would be met and overcome and the disk would flatten further on increasing τ (see AT86). At some point, though, this compression must stop.

Fig. 3c is interesting because it shows the disk approach the dilute energy balance as v_c is increased. The limiting $\varepsilon(\tau)$ curve in this case being that of Goldreich and Tremaine (1978) (cf. their Fig. 2). In the dense regime (low v_c) the injection of energy by the collisional stress source becomes important and so each collision must dissipate more energy than otherwise. This explains the low values of ε the energy balance requires when $v_c/v_b = 1$ and 0.25. .

Figs 4a and 4b present the nonlocal and local kinematic viscosity against τ . Here we find relatively good agreement with Salo (1991) for each v_c/v_b . As with the velocity dispersion, the kinetic treatment overestimates the viscosities, especially the nonlocal viscosity for larger ratios of v_c/v_b . Otherwise, the figure displays quite well, in the relative 'convexity' and 'concavity' of the curves,

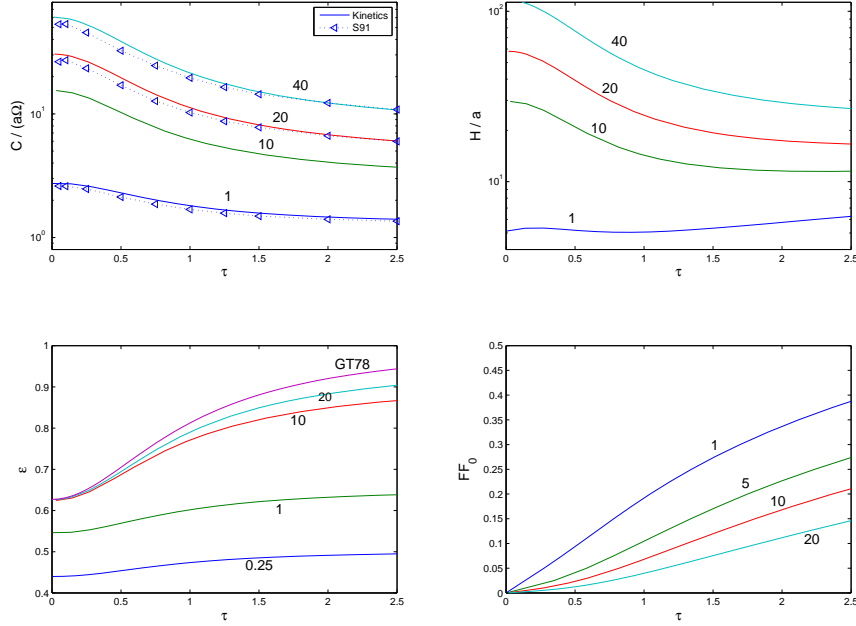


Fig. 3. Various equilibrium properties computed by a polytropic kinetic model ($\alpha = 0.9$) with a preaveraged ε (solid curves), and by the simulations of Salo (1991) which we denote by ‘S91’ (triangles). We employ different ratios of v_c/v_b (inserted adjacent to the relevant curve) but fixed $p = 0.234$. The quantities are plotted as functions of optical depth τ . The four panels correspond to: (a) equilibrium velocity dispersion C , (b) disk scale height H , (c) averaged equilibrium coefficient of restitution ε , and (d) central filling factor FF_0 . The Goldreich and Tremaine (1978) dilute disk energy balance is referred to as GT78 in subplot (c).

the different behaviours associated with the two regimes of disk — the warm and dilute on one hand, and the dense on the other.

In Fig 5 we plot the quantity $\tau\nu$, which is proportional to the angular momentum flux and hence a key indicator of the stability of the equilibrium. We present three interesting cases. The first, corresponding to $v_c/v_b = 20$, represents a ‘bimodal’ profile; such cases have been discussed by Hämeen Antilla (1982) and Spahn and Schmidt (2006), and were first revealed in simulations by Salo (1991). For low to middle τ the disk is in the dilute regime; there the angular momentum flux increases sharply and then gently decreases after reaching a turning point. As explored in Latter and Ogilvie (2006), the region of large positive slope does not lead to viscous overstability because the stress (dominated by the translational component) is nonlocal in time; however, the region of negative slope should give rise to the viscous instability. At high optical depths the disk enters the dense regime and the collision frequency becomes sufficiently large to engender a significant collisional stress: the angular momentum flux begins to increase gradually under its influence.

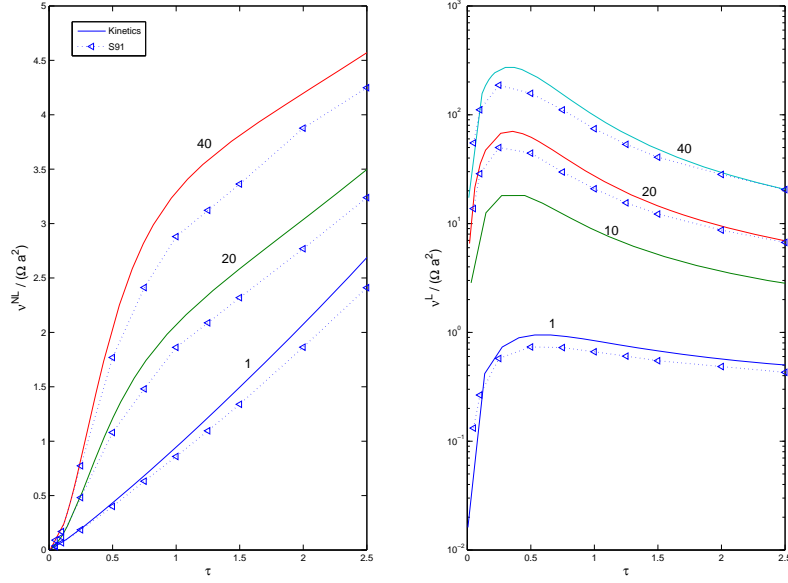


Fig. 4. Local and nonlocal components of the kinematic viscosity. Panel (a) presents the nonlocal component of the kinematic viscosity ν^{NL} , and (b) the local component of kinematic viscosity ν^L . As earlier different ratios v_c/v_b are employed with $p = 0.234$, and the solid curves represent the polytropic kinetics and the triangles Salo's simulations. Both viscosities are scaled by $a^2\Omega$.

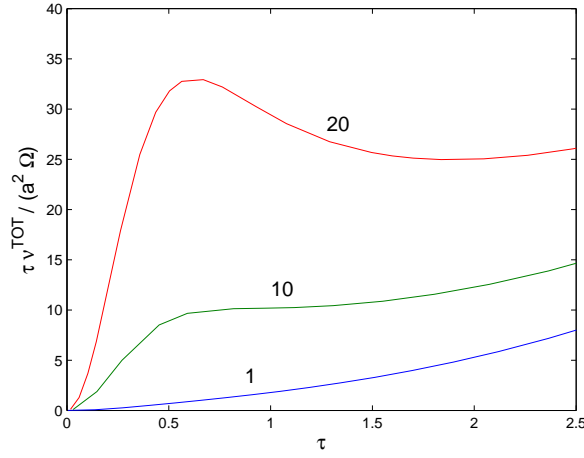


Fig. 5. The total angular momentum flux $\tau\nu = \tau(\nu^{NL} + \nu^L)$ versus τ at different ratios of v_c/v_b . The flux is scaled by Ωa^2 .

The second curve corresponds to $v_c/v_b = 10$, and it shows the collisional stress asserting itself at a lower τ , effectively negating the ‘window’ of decreasing angular momentum flux exhibited by the $v_c/v_b = 20$ curve. In this intermediate range the slope of the curve is near to zero as the opposite tendencies of the local and nonlocal stresses cancel. The disk is perhaps marginally stable to

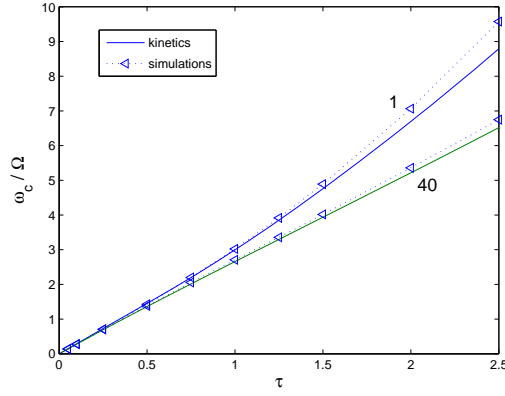


Fig. 6. The scaled collision frequency ω_c/Ω as a function of optical depth τ for two illustrative ratios of v_c/v_b .

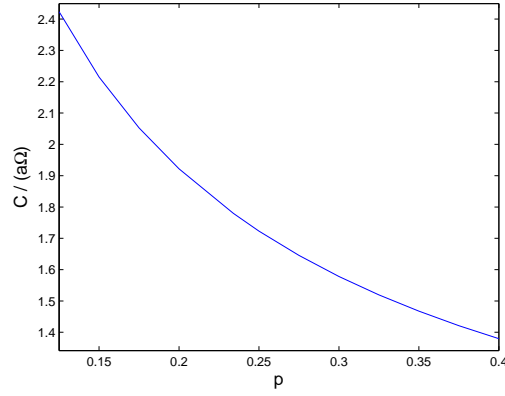


Fig. 7. The equilibrium velocity dispersion at $FF_0 = 0.2$ as a function of the exponent p with fixed $v_c = v_b$.

the viscous instability in this range.

The third curve corresponds to a disk which lies in the dense regime for all τ . Here ν is always dominated by the nonlocal component. In this case the angular momentum flux gradually increases and may at a critical τ possess a gradient sufficiently large to initiate the viscous overstability.

Fig. 6 plots the collision frequencies for two ratios, $v_c/v_b = 40$ and 1. These illustrate the dilute regime and the dense regime respectively. In the latter case ω_c clearly exhibits its linear dependence on τ , while the former shows a gentle superlinear dependence for sufficiently large τ , this mainly arising from the Enskog factor. The kinetic model uses expression (62) to evaluate the collision frequency. The matching between the two approaches is good in general, though at larger τ , there is an increasing discrepancy in the dense case.

Finally, in Fig. 7 we plot the variation of c with respect to the elasticity

exponent p for fixed $v_c = v_b$ and $\text{FF}_0 = 0.2$. The trend reveals that increasing p decreases the equilibrium velocity dispersion. This follows because an elasticity law with a larger p varies with impact velocity more steeply. With such a law, a collision characterised by a given impact velocity is more dissipative than if the slope were more shallow. If collisions are more dissipative in general then the equilibrium c may be smaller both to minimise the collision frequency and to maximise the injection of energy by the collisional stress.

3.9 Importance of vertical nonlocality

Having applied the kinetic model to equilibrium calculations, compared the properties computed with those from simulations, and discussed these properties more generally, we shall now test some of the assumptions it uses. First, we examine the approximation of vertical locality, introduced in Section 2.2.6.

In order to best test the assumption we present the equilibrium characteristics of two representative disks: one without self-gravity and one with self-gravity. These two cases correspond to relatively thick and thin disks, respectively, and hence the assumption of vertical locality will impact on each quite differently. Otherwise, the model incorporates

- a preaveraged ε , the piecewise power law, using (45) and (46) and with $p = 0.234$ and $R_c = 2$
- Gaussian vertical structure.

We employ Gaussian vertical structure because this model admits analytical vertical averages in the vertically nonlocal case, in contrast to the polytropic model (see Section 3.4). We believe the results we obtain with the Gaussian profile would also hold qualitatively in the polytropic case. Recall that the only change made by the assumption of vertical locality is omission of the ‘nonlocality factor’, $\exp[-(a^2/H^2)k_z^2]$ in the collision integrals.

First we set $G_s = 0$ and compute non-self-gravitating equilibria with and without vertical nonlocality. Selected equilibrium properties, as functions of FF_0 , are plotted in Fig. 8. The two models agree closely because of the relatively large scale height, H , plotted in Fig. 8b. This quantity is approximately 2.5 at its smallest; consequently, the ‘nonlocality factor’ varies at most between about 1 and 0.85, and much less at higher central filling factors. The discrepancy between the two models can then be at most some 15%, and it appears its effect is much less.

Next we set $G_s = 6.6$, a realistic value for solid ice particles in the B-ring. The equilibrium properties are plotted in Fig. 9, as before. The discrepancies between the two methods are more pronounced, and especially attending those

quantities most closely aligned with the vertical structure, τ and H . These two deviate substantially at large central filling factors as then the disk semithickness approaches a particle radius. For these very thin disks the ‘nonlocality factor’ can vary between 0.367 and 1 and thus play a significant role. However, we are encouraged by the agreement exhibited by the horizontal properties, such as velocity dispersion, which are not nearly as affected.

The reason why the vertical properties are more affected than the horizontal ones is because of the local model’s overestimation of the vertical collisional pressure P_{zz}^c in the height equation, which is where H and hence τ are determined effectively. In a very thin disk P_{zz}^c will be very small: most colliding particles are in the same plane and hence nearly all collisional momentum transport will lie in this plane. But the collisional dynamics of the local model is insensitive to the vertical stratification and hence to this fact. Evidence for this interpretation can be observed in Fig. 9b where we see the disk semithickness H increase at a lower FF_0 than it should because of the overestimation of the vertical momentum flux.

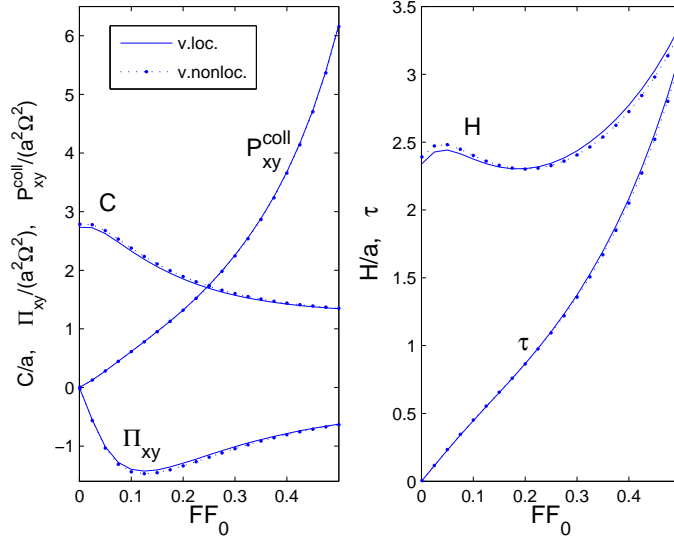


Fig. 8. Comparison between the vertically local model (the solid line) against the vertically nonlocal model (triangles) in a non-self-gravitating disk, $G_s = 0$. In (a) we plot selected ‘horizontal properties’ of the equilibria (C , P_{xy}^c , Π_{xy}), and in (b) the ‘vertical properties’ (H , τ). These are presented as functions of central filling factor FF_0 . Otherwise we have adopted Gaussian vertical structure and a preaveraged ε with $p = 0.234$ and $R_c = 2$.

In summary, however, the assumption of vertical locality is certainly justified. Very little error is introduced in disks which possess a $H \gtrsim 2a$, and the horizontal properties are approximated adequately in self-gravitating disks where the semithickness approaches a particle radius. It is only the optical depth τ and H itself in very thin disks that we must be careful interpreting when FF_0

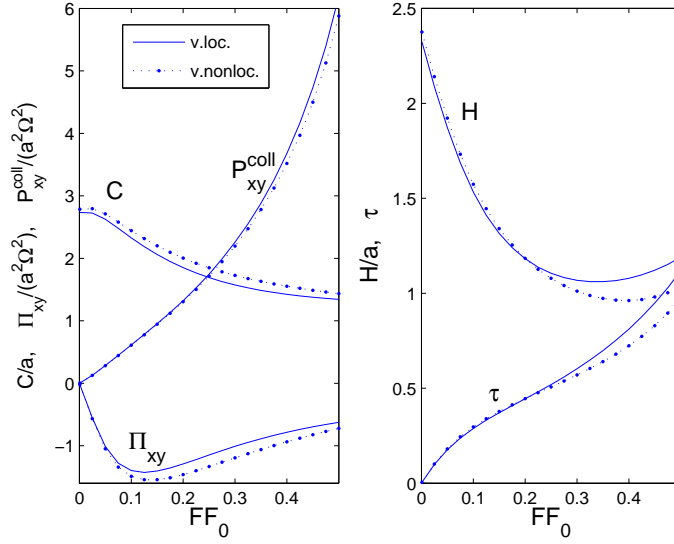


Fig. 9. As for Fig. 8 but for a self-gravitating disk, $G_s = 6.6$.

is high. This is pleasing because the assumption of vertical locality provides a number of mathematical advantages. Particularly useful is its decoupling of the height equation from the horizontal pressure tensor equations and the simplification of the integrands. These simplifications, also, are crucial in the polytropic model, and also in the interpolation, and expansion models, as they facilitate the complete integration of the collision terms.

3.10 Validity of preaveraged coefficient of restitution

In this section we test the preaveraging approximation against a model which incorporates the variation of ε consistently within the collision integrals. The coefficient of restitution is set as a straight power law: $\varepsilon = (\mathbf{g} \cdot \mathbf{k}/v_c)^{-p}$ where $v_c = 0.01 \text{ cm s}^{-1}$ and $p = 0.234$. This functional form supplies analytical expressions for both $\langle \varepsilon \rangle_q$ and $A_\gamma(\varepsilon)$. Expressions for the former are listed in (42) and (43) and the latter are simple power laws but with a slightly different ' v_c ' (we omit these expressions). Thus our choice of the straight power law ensures that the integrations we need to undertake are only two-dimensional and not three, as would be the case for the piecewise function. In addition we set the velocity scale $a\Omega = 0.02 \text{ cm s}^{-1}$ and $G_s = 0$. Otherwise, the model assumptions are

- polytropic vertical structure with $\alpha = 0.9$
- vertical locality

In Fig. 10 we plot selected equilibrium properties. The agreement is quite good generally and excellent for the collisional stress. The preaveraged model

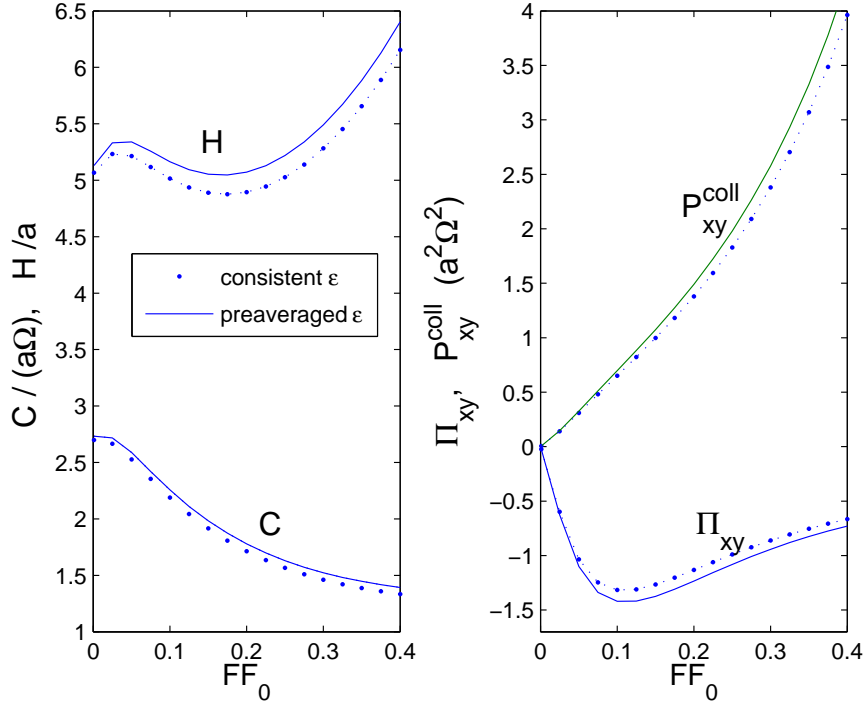


Fig. 10. Selected equilibrium properties as computed by a model which incorporates a preaveraged ε and a model that allows ε to vary within the collision integrals. A straight power law was adopted for ε , with $p = 0.234$ and $R_c = 2$. The quantities H and C appear in panel (a), and the collisional and translational stresses P_{xy}^c and Π_{xy} in panel (b). The vertical structure is assumed to be polytropic.

slightly overestimates the equilibrium velocity dispersion and collisional pressure tensor. Overall, however, these results reveal that this approximation gives excellent qualitative and good quantitative agreement.

3.11 Interpolation model

Finally, we investigate the interpolation model introduced in Section 2.2.8 and worked out in detail in Appendix A. The F functions were interpolated on the range $\xi \in [-0.75, 0.75]$ with a mini-max method which returned a relative error of at most 3%. The F_{ij} which appear in Eqs (47) were computed as

$$\begin{aligned}
 F_{11} &= 1.9619, & F_{12} &= 5.3174, & F_{13} &= 6.545, & F_{14} &= 3.5450, \\
 F_{21} &= 1.0000, & F_{22} &= 1.7725, & F_{23} &= 0.9352, \\
 F_{31} &= 1.7725, & F_{32} &= 4.5401, & F_{33} &= 3.5450
 \end{aligned}$$

(to 4 decimal places). Also we assume

- polytropic vertical structure with $\alpha = 0.9$,

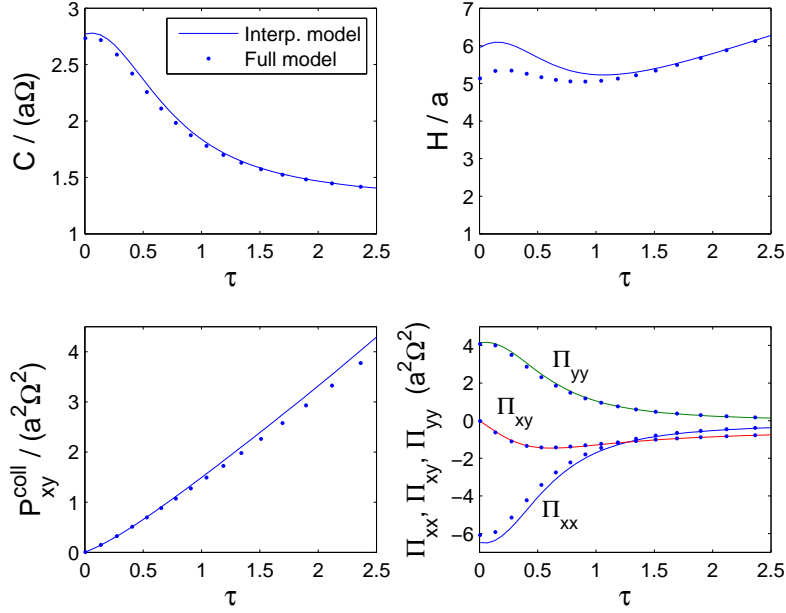


Fig. 11. Selected equilibrium properties as functions of τ computed by the full model (points) and the interpolation model (solid line). Both models adopt polytropic vertical structure ($\alpha = 0.9$) and a preaveraged ε with $p = 0.234$ and $R_c = 2$. The velocity dispersion C is plotted in panel (a), the semithickness H in (b), the collisional stress P_{xy}^c in (c), and components of the translational stress Π in (d)

- vertical locality,
- a piecewise power law, which is preaveraged with $p = 0.234$ and $R_c = 2$

Because the collision integrals are linear in \mathbf{a} the equilibrium problem is greatly simplified. We can solve Eqs (48)-(51) analytically for the xx , xy and yy components of \mathbf{a} , leaving a single nonlinear algebraic equation for c in terms of the governing parameters, τ , R_c , p , G_s . The equilibrium calculation is then rapidly completed by a one-dimensional Newton-Raphson algorithm.

A comparison of the equilibrium properties as computed by the interpolation and exact method are presented in Fig. 11. The agreement here is good throughout the full range of τ which is somewhat surprising: we expected discrepancies near $\tau = 0$ arising from the truncation in anisotropy (\mathbf{a}). Perhaps this accounts for the deviation of disk semithickness H at low τ , but it is puzzling that this vertical property is singled out. In general, given the truncation in \mathbf{a} , the excellent agreement for general τ suggests that dense rings exhibit a level of anisotropy which can be captured adequately by a linear model.

Because this method reduces the collision integrals to algebraic expressions (albeit complicated), more advanced linear and nonlinear analyses of the ring kinetics are easier to undertake. Moreover, its success in equilibrium calcula-

tions encourages its application in these investigations.

4 Linear stability

Now that the statistics of the dense disk equilibrium have been established, we shall examine its response to small perturbations. Our interest is principally in the growth rates and stability of the overstable modes as functions of the kinetic parameters. We will not supply an exhaustive survey in this paper but rather illustrate the principal features while also touching on a comparison with the simulations of Salo *et al.* (2001).

4.1 Linearised equations

The disk admits steady homogeneous solutions characterised by the constant optical depth τ_0 and velocity dispersion tensor \mathbf{W}^0 . Suppose that we perturb these equilibria with an infinitesimal axisymmetric disturbance

$$\begin{aligned}\tau &= \tau_0 + \tau'(x, t), \\ \mathbf{u} &= -(3\Omega x/2)\mathbf{1}_y + \{u(x, t)\mathbf{1}_x + v(x, t)\mathbf{1}_y\}, \\ \mathbf{W} &= \mathbf{W}^0 + \mathbf{W}'(x, t), \\ \Phi_D &= \Phi_D^0 + \Phi_D'(x, t),\end{aligned}$$

The system is subsequently nondimensionalised along the following lines: time with respect to Ω^{-1} , space with respect to C_0/Ω , velocity with C_0 , and velocity dispersion tensor with C_0^2 . We now use the nondimensionalised quantities but with no change in notation.

The linearised equations read

$$\partial_t \tau' = -\tau_0 \partial_x u, \quad (63)$$

$$\partial_t u = -\partial_x \Phi' + 2v - \partial_x [W'_{xx} + (P'_{xx}/N)'] - \frac{1}{\tau_0} (W_{xx} + P_{xx}^c/N)_0 \partial_x \tau', \quad (64)$$

$$\partial_t v = -\frac{1}{2} u - \partial_x [W'_{xy} + (P'_{xy}/N)'] - \frac{1}{\tau_0} (W_{xy} + P_{xy}^c/N)_0 \partial_x \tau', \quad (65)$$

$$\partial_t W'_{xx} = -2W_{xx}^0 \partial_x u + 4W'_{xy} + (Q_{xx}/N)', \quad (66)$$

$$\partial_t W'_{xy} = -W_{xy}^0 \partial_x u - W_{xx}^0 \partial_x v + 2W'_{yy} - \frac{1}{2} W'_{xx} + (Q_{xy}/N)', \quad (67)$$

$$\partial_t W'_{yy} = -2W_{xy}^0 \partial_x v - W'_{xy} + (Q_{yy}/N)', \quad (68)$$

$$\partial_t W'_{zz} = (Q_{zz}/N)', \quad (69)$$

where the perturbed collision terms, Q'_{ij} and $(P^c_{ij})'$, are expressed in the form

$$Q'_{ij} = \left(\frac{\partial Q_{ij}}{\partial \tau} \right)_0 \tau' + \left(\frac{\partial Q_{ij}}{\partial W_{xx}} \right)_0 W'_{xx} + \left(\frac{\partial Q_{ij}}{\partial W_{xy}} \right)_0 W'_{xy} \\ + \left(\frac{\partial Q_{ij}}{\partial W_{yy}} \right)_0 W'_{yy} + \left(\frac{\partial Q_{ij}}{\partial W_{zz}} \right)_0 W'_{zz} + \left(\frac{\partial Q_{ij}}{\partial e_{xx}} \right)_0 e'_{xx} + \left(\frac{\partial Q_{ij}}{\partial e_{xy}} \right)_0 e'_{xy},$$

and e_{ij} is the rate of strain tensor. To these we add the perturbed Poisson equation, in order to obtain Φ' , and the perturbed height equation, in order to relate the perturbed central filling factor FF'_0 with τ' .

Once we express the radial perturbation as Fourier modes $\propto \exp(ikx + st)$, we let the nondimensionalised solution of the linearised Poisson equation take the form

$$\Phi'_D = -\frac{2g}{|k|} \tau' \quad (70)$$

(Binney and Tremaine, 1987), where

$$g = \left(\frac{m G}{a^3 \Omega} \right) \left(\frac{a \Omega}{C_0} \right) = G_s R, \quad (71)$$

and is equal to $(Q\tau_0)^{-1}$, where Q is the Toomre parameter. Once this is substituted we obtain a seventh order algebraic eigenvalue problem for the growth rate s . This in turn supplies a seventh order dispersion relation of the same structure as Eq. (25) in Latter and Ogilvie (2006), but in which the coefficients are functions of G_s , g , k , the equilibrium values of \mathbf{W} and \mathbf{P}^c , and the derivatives of \mathbf{W} and \mathbf{P}^c . If we adopt the general dense formalism devised in Section 2.2.6, evaluating these coefficients requires the numerical calculation of a number of surface integrals and their derivatives.

Before continuing, we will say a few words about the parameter g given by Eq. (71). Though it appears that g simply derives from the quantities G_s and R , a quick calculation shows that it can take large values in a typical dense equilibrium, and hence Q can take very low values. For example, if $G_s = 6.6$, $a = 1$ m, $\tau \approx 1$ and $C/(a\Omega) \approx 1.5$ (see Fig. 9), we compute $Q \approx 0.23$. Kinetic models characterised by these low values of Q exhibit viscous overstability on arbitrarily short scales. Some aspects of this issue have been examined in Latter and Ogilvie (2006) in the context of viscous instability. Part of the problem originates in the small velocity dispersion of axisymmetric self-gravitating equilibria, an admittedly artificial scenario. A real self-gravitating disk will be subject to non-axisymmetric instability for a Q less than about 2, and the recurrent wake structures it engenders will heat the disk sufficiently to keep Q above unity. In addition, gravitational scattering and focusing (effects we neglect) will supply extra heat sources. Self-gravitating simulations bear out these point and show that Q is typically unity or higher (Salo, 1992a). The second important issue is our omission of the third order moments which

are important on short scales and which should extinguish instability. These considerations will not be addressed in this paper, but we will revisit it in a future nonlinear axisymmetric study where a solution to this problem is more urgent.

4.2 Results

The model we employ incorporates

- polytropic vertical structure with $\alpha = 0.9$,
- vertical locality, and
- a preaveraged piecewise power law for ε .

Both the equilibrium and its linear stability depend on six parameters: τ_0 , p , a , m , Ω , and v_c , all of which can be determined by observation or experiment. The nondimensionalised system is parametrised by the dimensionless quantities τ , p , R_c and G_s .

The perturbed collision terms depends on the perturbations of FF_0 via the Enskog factor. But this must be related to the other perturbations before we can proceed. The relevant equation can be obtained via (58):

$$\begin{aligned} \text{FF}'_0 = \frac{1}{H_0 + \text{FF}_0(\partial H/\partial \text{FF})_0} & \left\{ \frac{4\Gamma(\alpha + \frac{3}{2})}{3\sqrt{\pi}\Gamma(\alpha + 1)} \tau' - \text{FF}_0 \left[\left(\frac{\partial H}{\partial W_{xx}} \right)_0 W'_{xx} \right. \right. \\ & + \left(\frac{\partial H}{\partial W_{xy}} \right)_0 W'_{xy} + \left(\frac{\partial H}{\partial W_{yy}} \right)_0 W'_{yy} \\ & \left. \left. + \left(\frac{\partial H}{\partial W_{zz}} \right)_0 W'_{zz} + \left(\frac{\partial H}{\partial e_{xx}} \right)_0 e'_{xx} + \left(\frac{\partial H}{\partial e_{xy}} \right)_0 e'_{xy} \right] \right\}. \end{aligned}$$

This equation, which relates the perturbations of FF_0 , H and τ , conveys information pertaining to vertical disk structure into the linear dynamics via the equilibrium H and its derivatives. In particular, it introduces vertical self-gravity into the problem. Self-gravity also appears in the x component of the momentum equation, (64).

Once the linearised equations are sorted, our procedure is to step through FF_0 , evaluate the equilibrium at each point and obtain the dispersion relation, which is then solved for various k (or wavelength). We perform three runs:

- without self-gravity in either the height equation or in the momentum equation, Fig. 12;
- with self-gravity in the height equation alone (thereby modelling only its enhancement of the vertical restoring forces), Fig. 13;
- with self-gravity in both equations, Fig. 14.

The algorithm evaluates the growth rates of the seven linear modes discussed in Latter and Ogilvie (2006). These are: the two potential viscous overstable modes, the potential viscous instability mode, the energy mode, the two potential anisotropic overstable modes, and the relaxation mode. We, however, concentrate on the two potentially overstable ones (left and right-going waves). First, their curves of marginal stability are plotted in the (τ, λ) plane, where $\lambda = 2\pi/k$ is wavelength. Then, to these we add the curves of constant growth or decay, which we truncate as they collapse onto the line of marginal stability.

We adopt the Bridges *et al.* (1984) elasticity law, so as to compare with the simulations of Salo *et al.* (2001); thus $p = 0.234$ and $v_c = 0.0077 \text{ cm s}^{-1}$. The particles are assumed to possess radii of 100 cm and the shearing sheet is located at a radius of 100,000 km. As a result $a\Omega = 0.0195 \text{ cm s}^{-1}$ and $R_c = a\Omega/v_c = 2.53$. We vary G_s so as to compare our results with the simulations, in which the particles' internal density took several values less than 900 kg m^{-3} (solid ice). In addition, Salo *et al.* conducted a number of simulations where the vertical component of self-gravity was mimicked by an enhancement of the particles' vertical epicyclic frequency, Ω_z . The effective G_s associated with such an enhancement cannot be readily determined, though we have the estimate

$$\Omega_z^2 = \Omega^2 + (\partial_z^2 \phi_D)_{z=0} \approx \Omega^2 (1 + 3G_s \text{FF}_0), \quad (72)$$

in which it has been assumed that ϕ_D varies much slower with x than with z . Typically, Salo *et al.*'s simulations set $\Omega_z/\Omega = 3.6$ which corresponds to very large G_s , especially for low FF_0 . When FF_0 is about 0.3, G_s is still greater than 10. This is surely an overestimate, and Eq. (72) should be treated with some caution.

4.2.1 Growth rates

We find that a non-self-gravitating disk is stable to the viscous instability for all the optical depths we examine: $0 < \tau < 5$. This conforms with the dense gas N -body simulations. Above a critical τ the viscous overstability occurs. This value is approximately $\tau = 2.5$ which corresponds to a central filling factor of 0.375 (cf. Fig. 12). In contrast, the N -body simulations of Salo find overstability only for very high optical depths, of order 4. This disagreement is not unexpected: high filling factor disks in monodisperse simulations can 'relax' their close packing via the formation of layers or 'sheets'. Such disks, as a consequence, can possess filling factors below the critical level of overstability, despite being quite optically thick.

The stability curves of the long modes differ very little from each other: once the critical τ is reached nearly all the overstable modes become unstable, which mirrors the hydrodynamical stability curves of Schmidt *et al.* (2001). As the disk makes the transition to instability, modes on lengths of some 200

m will grow fastest. The shortest overstable scales are approximately 80—90 m. These are a little longer than usually predicted by hydrodynamics and simulations.

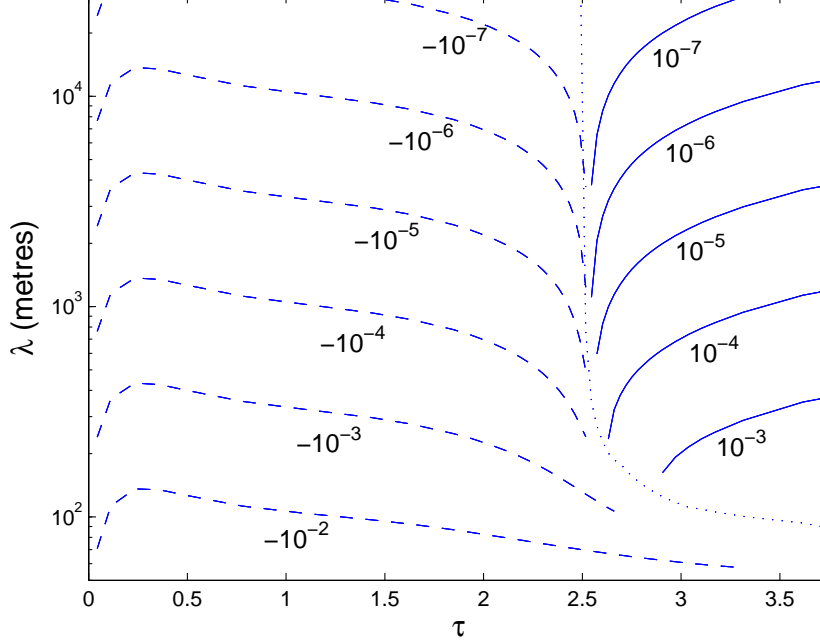


Fig. 12. The curves of constant growth and decay rates, $\text{Re}(s)$, for the overstable modes in the (τ, λ) plane in a non-self-gravitating disk ($G_s = 0$, $g = 0$). The model adopts polytropic vertical structure and a pre-averaged ε with $p = 0.234$ and $R_c = 2.53$. Negative growth rates are plotted with dashed lines and positive growth rates with solid lines. The curve of marginal stability, $\text{Re}(s) = 0$, is the dotted line.

In order to examine the contribution of the vertical component of self-gravity we set $G_s = 3.0$ in the height equation, but zero in the momentum equation. This captures the vertical compression caused by self-gravity (and the subsequent increase in collision frequency and its rate of change) but will not alter the structure of the dispersion relation. The value adopted for G_s corresponds to internal particle densities of $\rho_p = 408 \text{ kg m}^{-3}$, which is less than solid ice but is illustrative nonetheless.

The curves of constant growth and decay are plotted in Fig. 13. These are similar to those in Fig. 12; the chief difference lies in a shift to lower optical depths and slightly shorter scales. The critical τ in this case is ≈ 1.15 and the critical FF_0 approximately 0.335.

The fastest growing modes at the stability transition are now on scales of about 150—200 m, and the shortest affected scales are about 60—70 m. These agree a little closer with the generic hydrodynamic profiles.

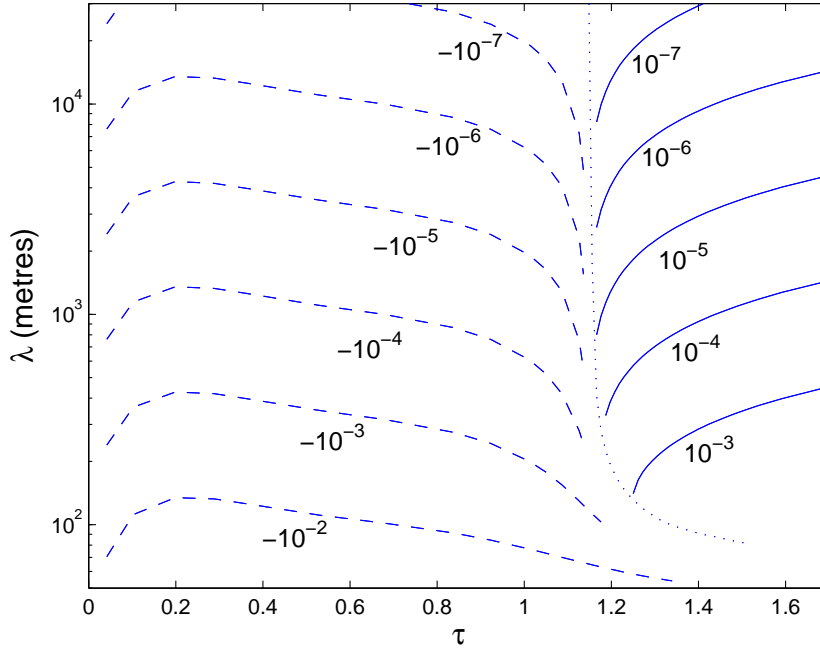


Fig. 13. The curves of constant growth and decay rates $\text{Re}(s)$ for the overstable modes in the (τ, λ) plane, in a disk where self-gravity is included in the height equation but not elsewhere. We have set $G_s = 3$ and $g = 0$.

Next we include self-gravity in both the height equation and in the x component of the momentum equation. We seek to compare directly with the self-gravitating run of Salo *et al.* in which $\rho_p = 225 \text{ kg m}^{-3}$. Therefore, $G_s = 1.65$ by Eq. (56) and g takes the appropriate value from Eq. (71). The subsequent curves of constant growth and decay are plotted in Fig. 14.

With the addition of self-gravity in the momentum equation it is the intermediate lengthscales ($\sim 100 \text{ m}$) which become unstable first, as illustrated by the pronounced salient in the curve of marginal stability. The longest wavelengths are unaffected. On the other hand, decreasing G_s from 3 to 1.65 increases the critical τ of overstability on the longest scales, from about 1.15 to approximately 1.43 (which corresponds to a central filling factor of 0.34). In contrast, the lowest critical τ for overstability on the intermediate scales is about 1.23 (for $\lambda \approx 100 \text{ m}$).

These results are in good agreement with the simulations, which find that overstability begins at approximately 1.2 (see Fig 5a in Salo *et al.*, 2001) and on scales of 100–150 m. This conformity contrasts with the poor agreement in the non-self-gravitating run and proceeds essentially from the introduction of the vertical self-gravity. In simulations the self-gravity negates, to some extent, the relaxation of packing fraction and allows the higher filling factors necessary for overstability. It thus removes the obstacle that prevented the

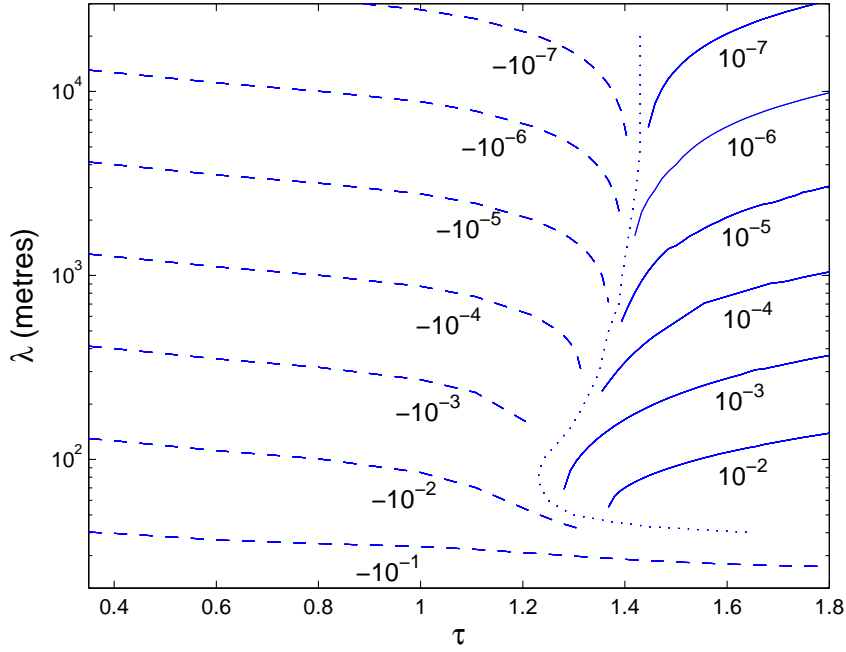


Fig. 14. The curves of constant growth rate $\text{Re}(s)$ for the overstable modes in the (τ, λ) plane, in the case when self-gravity is properly included in both height and momentum equations. Here $G_s = 1.65$ and $g = G_s R$, cf. Eq. (71).

kinetic model and the simulations agreeing.

Finally we set $G_s = 6.6$, corresponding to solid ice particles, $\rho_p = 900 \text{ kg m}^{-3}$. The parameter g was set to its appropriate value from (71), and thus the Toomre parameter was generally very small. The critical τ is now shifted to about 0.8 for long scales and somewhat less for intermediate scales. As mentioned earlier, in Section 4.1, we find that the overstability is not quenched on the short scales, thus the ‘bulge’ in the stability curve associated with self-gravity (cf. Fig. 14) extends down to lengths of a particle radius. This behaviour is surely unphysical and derives not only from the small Q but also the omission of the third order moments in the pressure tensor equation.

4.2.2 Marginal curves

Finally we let the elastic properties of the particles vary by letting p and the parameter $R_c = a\Omega/v_c$ take other values. Marginal curves of $\text{Re}(s) = 0$ for viscous overstability are computed in (p, τ) space for given k and R_c for a self-gravitating disk with $G_s = 6.6$ but with $g = 0$. These curves are obtained from a simple (but robust) bisection root-finding method. Fig. 15 plots three illustrative curves for a mode with $k = 0.01$, which corresponds roughly to $\lambda = 600 \text{ m}$. The parameter R_c takes the values 2.53, 0.67, and 0.25. The first

two correspond to 100 cm size particles at a radius of 100,000 km in the B-ring with the elasticity data of Bridges *et al.* (1984) and Supulver *et al.* (1995) respectively.

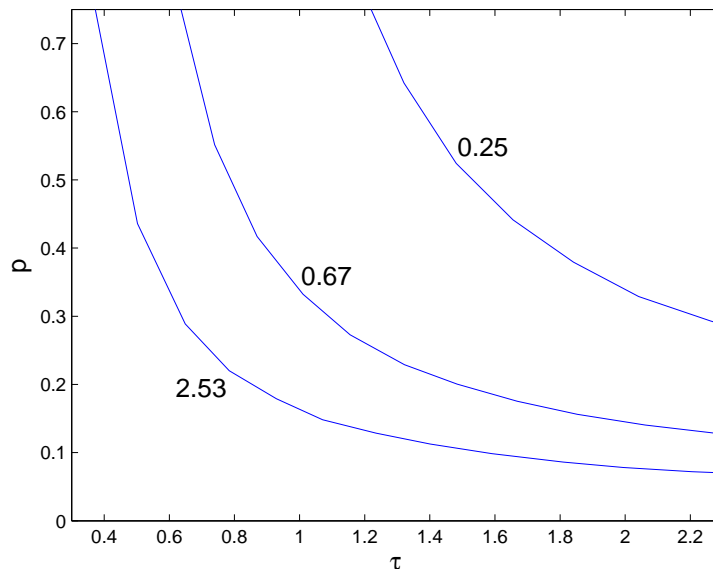


Fig. 15. Marginal curves of overstability in the (p, τ) plane for $k = 0.01$, $G_s = 6.6$ and various $R_c = a\Omega/v_c$. Regions above the curves are overstable, regions below are stable.

The stability trend here is easy to interpret: the larger τ , p , and R_c the more vulnerable the disk to viscous overstability. The last correlation derives from the fact that the greater R_c the more important the background shear flow, and consequently the greater the collisional viscous stress. As $R_c \rightarrow 0$ the nonlocal contributions vanish. The effect of p lies in its control of the equilibrium disk velocity dispersion. The larger p the lower C , and hence the more important the collisional viscous stress (cf. Fig. 7).

Another fact to note is the sensitivity of the critical τ to the elasticity laws. The Bridges *et al.* data (for which $p = 0.234$) gives a critical τ of roughly 0.8, but the Supulver *et al.* data (for which $p = 0.19$) gives a value nearer to 1.5. In contrast, in these two cases and more generally, the critical FF_0 does not change as dramatically and lies somewhere in the interval 0.32–0.375. We conclude that the viscous overstability responds essentially to a sufficiently large filling factor, the critical value of which does not vary significantly with respect to the collision law (or self-gravity). It rather than τ is the key parameter governing the onset of instability.

Though the stability results presented in Fig. 15 hold only for a mode of length some 600 m, the stability of all the scales should follow qualitatively the same trend, irrespective of the precise value of G_s and g . Indeed these results are

consistent with the self-gravitating simulations of Salo *et al.* (2001) when they vary R_c (cf. their Fig. 5b).

Given that optical depth is a key observational property, and that it depends so delicately on the elastic properties of the particles, our detailed model is a useful first step in constraining the collisional parameters of ring particles. Certainly the model needs refining, particularly with respect to self-gravity, but it does provide an account of dynamical processes which can be compared directly with observations. Studies such as Salo and Karjalainen’s (2003) combined dynamical and photometric modelling have already made inroads into such comparisons.

5 Conclusion

In summary, we have developed a workable formalism with which to attack the dynamics of a dense ring, one in which the collisional transport/production processes and filling factor effects are fully included, as is the dependence of ε on impact velocity. The model both simplifies and generalises the work of AT86 and as a consequence encourages us to conduct more advanced dynamical analyses.

The theory is founded on that of Enskog kinetics and thus shares its assumptions regarding the neglect of ternary or higher collisions and the modelling of space and velocity correlations. An additional assumption is the limiting of the velocity dispersion’s spatial variation to scales significantly longer than a particle radius (i.e. vertical isothermality). Also the velocity distribution is assumed to be a triaxial Gaussian, and the vertical structure of the number density to take a predetermined form, either a Gaussian or a polytrope. The theory must be supplemented, with the functional forms of the Enskog factor and the coefficient of restitution.

The full model can be further simplified if additional assumptions are made, such as those of locality in density, a preaveraged coefficient of restitution, or if the collision integrands are interpolated and anisotropy assumed small. Each of these models fared well in comparisons with the exact approach (Sections 3.9 — 3.11). Thus we employed them generally.

We undertook a comparison of equilibria computed by the kinetics of Araki and Tremaine (1986) and the simulations of Wisdom and Tremaine (1988) and Salo (1991). The former two comparisons exposed the shortcomings of the Gaussian model of vertical structure at moderate and high central filling factors in monodisperse disks, and revealed an error in the numerical implementation of the Araki and Tremaine model. It was also shown that a

polytropic model of vertical structure performed well in these regimes and acceptably at lower filling factors.

The polytropic kinetic model was tested in equilibrium calculations against the results of Salo’s (1991) N -body simulations. Overall the agreement was good, with the major discrepancies within the range of error introduced by the various approximations.

Next we probed the linear theory of the kinetic model and reproduced qualitatively much of the behaviour presented by the particle simulations of Salo *et al.* (2001). We find that without self-gravity a disk composed of 100 cm radius particles exhibits viscous overstability at a critical optical depth of about 2.5. This is a significantly lower value than Salo *et al.*’s, which is approximately 4, and proceeds essentially from the kinetic model’s insistence on a fixed vertical structure. A simulation can ‘relax’ its close packing by the formation of vertical sheets and thus remain below the critical filling factor necessary to instigate overstability. (Note however that the sheets are artefacts of a monodisperse model and hence unrealistic.) This discrepancy vanishes when self-gravity is properly included and agreement between theory and simulations is quite good for comparatively light particles. In this case modes of 100 m are the most unstable and possess a critical optical depth of about 1.23. In general, inclusion of the vertical component of self-gravity decreases the critical optical depth above which overstability manifests, while inclusion of the radial component of self-gravity induces overstability preferentially on intermediate scales, while leaving the longest scales untouched.

When the self-gravity is large, for instance when particles are as dense as solid ice, the linear dynamics on short scales is incorrectly described. The viscous overstability then extends to lengths of about a particle radius, which is unphysical. This arises because of the omission of third order moments from the pressure tensor equations and also because of the very low velocity dispersions which characterise axisymmetric disks in which gravitational collisions have been neglected. In reality, non-axisymmetric wakes, and gravitational collisions, warm the disk sufficiently and on short scales ‘thermal diffusion’ extinguishes instability. This issue must be addressed more fully in future nonlinear studies which employ the kinetic model and assume axisymmetry.

Within the model assumptions, we predict that overstability can occur at any radius of Saturn’s rings provided the optical depth exceeds a critical value. This value depends rather sensitively on the parameters of the collision law, in our case p and v_c ; in the B-ring, a plausible range of critical τ is between 0.8 and 1.6 (cf. Fig. 15). It must be said, however, that these estimates omit the effects of the gravitational wakes and size distribution both of which militate against the overstability’s onset. Even so, the dense B-ring seems the most likely place in which overstability occurs, as it exhibits unambiguously high optical

thicknesses. Finescale structure in such optically thick regions we conclude should be associated with this instability.

Our kinetic model could be developed in a number of ways. For instance, it would be straightforward, though tedious, to include the spin degrees of freedom and, possibly, size distribution. In the former case, we may use similar techniques to simplify the spin collision integrals. If a similarly workable formalism was developed we could examine, amongst a great many things, the action of particle spin on the onset of the overstability. Simulations have already begun probing this problem and await a kinetic comparison (Morishima and Salo, 2006). However, it should be noted that at present the frictional properties of ring particles are poorly understood. Also, the effect of gravitational encounters between particles should also be included. This is an important but difficult task. At present the model omits this important heating mechanism and thus underestimates the velocity dispersion of self-gravitating equilibria.

There are a numerous ring-related problems on which the full or interpolation formalism could be put to use immediately. The most obvious is the nonlinear saturation of the viscous overstability. The seven evolutionary equations could be numerically simulated to investigate the long-term evolution of the instability and how the elasticity parameters influence the statistics of the quasi-steady state to which it leads. The damping of nonlinear density waves launched by moons such as Prometheus, Pandora, etc could also be studied, as well as the wavy edges and wakes induced by Daphnis and Pan in the Keeler and Encke gaps. Theoretical models and their predictions have suffered from an approximate description of the viscosity in the ring. The full dense gas model could supply a more correct account of these effects. These would be formidable computational problems as at each time step and each spatial grid point we would need to evaluate a number of two-dimensional integrals. Such projects may best be tackled with the interpolation model with its algebraic expressions for the collision terms. That said continuum models, such as those we develop here, can reach the longer length and time scales necessary to fully describe the nonlinear behaviour. N -body methods are still too computationally intensive, particularly when self-gravity is added, to feasibly capture these scales.

Acknowledgements

We are extremely grateful to the referees Juergen Schmidt and Heikki Salo for their thorough checking of the manuscript. We also thanks them for the computational results they made available to us in the process of revision. HNL acknowledges funding from the Cambridge Commonwealth Trust, Trinity College Cambridge, and STFC.

6 Appendix: Interpolated collision terms

Presented here are the collision terms computed from the interpolation method to order \mathbf{a} . We have:

$$\mathbf{q} = \frac{2}{\pi} a^2 (1 + \varepsilon) \tilde{Y} [(1 + \varepsilon) \mathbf{L}_1 - 2 \mathbf{L}_2] \quad (73)$$

where the \mathbf{L}_1 tensor is defined by

$$\begin{aligned} \mathbf{L}_1 = 4\pi c^3 \left\{ F_{10} \left(\frac{1}{3} \mathbf{I}_2 + \frac{3}{10} \mathbf{I}_4 : \mathbf{a} \right) - \frac{a}{c} F_{11} \left(\frac{1}{5} \mathbf{I}_4 : \mathbf{e} + \frac{1}{7} \mathbf{I}_6 : \mathbf{a} : \mathbf{e} \right) \right. \\ \left. + \frac{a^2}{c^2} F_{12} \left(\frac{1}{7} \mathbf{I}_6 : \mathbf{e}^2 + \frac{1}{18} \mathbf{I}_8 : \mathbf{a} : \mathbf{e}^2 \right) - \frac{a^3}{c^3} F_{13} \left(\frac{1}{9} \mathbf{I}_8 : \mathbf{e}^3 \right) \right\}. \end{aligned}$$

and the \mathbf{L}_2 tensor by

$$\begin{aligned} \mathbf{L}_2 = 4\pi c^3 \left\{ \frac{2}{3} F_{30} \left(\mathbf{I}_2 + \frac{6}{5} \mathbf{a} \right) - \frac{2a}{15c} F_{31} (\mathbf{a}\mathbf{e} + \mathbf{e}\mathbf{a} + 2\mathbf{e} + \text{Tr}(\mathbf{e})\mathbf{a} + \text{Tr}(\mathbf{e})\mathbf{I}_2) \right. \\ \left. \frac{a^2}{105c^2} F_{32} \left(8[\mathbf{e}^2\mathbf{a} + \mathbf{a}\mathbf{e}^2] + 4\text{Tr}(\mathbf{e})[\mathbf{e}\mathbf{a} + \mathbf{a}\mathbf{e}] + 2[\text{Tr}(\mathbf{e})^2 + 2\text{Tr}(\mathbf{e}^2)]\mathbf{a} \right. \right. \\ \left. \left. + 30\mathbf{I}_6 : \mathbf{e}^2 - \frac{35}{3} \mathbf{I}_8 : \mathbf{a} : \mathbf{e}^2 \right) \right\}. \end{aligned}$$

The F_{ij} are pure numbers which are determined from the interpolation method and interpolation range; \mathbf{I}_2 is the rank 2 identity tensor and the other tensors

are defined through

$$\begin{aligned}
\mathbf{I}_4 : \mathbf{a} &= \frac{2}{3} \mathbf{a}, \\
\mathbf{I}_4 : \mathbf{e} &= \frac{2}{3} \mathbf{e} + \frac{1}{3} \text{Tr}(\mathbf{e}) \mathbf{I}_2, \\
\mathbf{I}_6 : \mathbf{a} : \mathbf{e} &= \frac{2}{15} \{ 2(\mathbf{a}\mathbf{e} + \mathbf{e}\mathbf{a}) + \text{Tr}(\mathbf{e})\mathbf{a} + \text{Tr}(\mathbf{e}\mathbf{a})\mathbf{I}_2 \}, \\
\mathbf{I}_6 : \mathbf{e}^2 &= \frac{1}{15} \{ 8\mathbf{e}^2 + 4\text{Tr}(\mathbf{e})\mathbf{e} + \text{Tr}(\mathbf{e})^2 \mathbf{I}_2 + 2\text{Tr}(\mathbf{e}^2) \mathbf{I}_2 \}, \\
\mathbf{I}_8 : \mathbf{a} : \mathbf{e}^2 &= \frac{2}{105} \{ 8(\mathbf{a}\mathbf{e}^2 + \mathbf{e}\mathbf{a}\mathbf{e} + \mathbf{e}^2 \mathbf{a}) + 4\text{Tr}(\mathbf{e})(\mathbf{a}\mathbf{e} + \mathbf{e}\mathbf{a}) \\
&\quad + 4\text{Tr}(\mathbf{a}\mathbf{e})\mathbf{e} + [\text{Tr}(\mathbf{e})^2 + 2\text{Tr}(\mathbf{e}^2)]\mathbf{a} + 2\text{Tr}(\mathbf{e})\text{Tr}(\mathbf{a}\mathbf{e})\mathbf{I}_2 + 4\text{Tr}(\mathbf{e}\mathbf{a}\mathbf{e})\mathbf{I}_2 \} \\
\mathbf{I}_8 : \mathbf{e}^3 &= \frac{1}{105} \{ 48\mathbf{e}^3 + 24\text{Tr}(\mathbf{e})\mathbf{e}^2 + 6[\text{Tr}(\mathbf{e})^2 + 2\text{Tr}(\mathbf{e}^2)]\mathbf{e} \\
&\quad + [\text{Tr}(\mathbf{e})^3 + 8\text{Tr}(\mathbf{e}^3) + 6\text{Tr}(\mathbf{e})\text{Tr}(\mathbf{e}^2)]\mathbf{I}_2 \}.
\end{aligned}$$

The collision momentum flux tensor is

$$\begin{aligned}
\mathbf{p}^c &= 8\sqrt{\pi}(1 + \varepsilon)\tilde{Y} a^3 c^2 \left\{ F_{20} \left(\frac{1}{3} \mathbf{I}_2 + \frac{1}{5} \mathbf{I}_4 : \mathbf{a} \right) \right. \\
&\quad \left. - \frac{a}{c} F_{21} \left(\frac{1}{5} \mathbf{I}_4 : \mathbf{e} + \frac{1}{14} \mathbf{I}_6 : \mathbf{a} : \mathbf{e} \right) + \frac{a^2}{7c^2} F_{22} \mathbf{I}_6 : \mathbf{e}^2 \right\}.
\end{aligned}$$

If the F_{jn} are set to zero except for $F_{10} = 2$, $F_{20} = \sqrt{\pi}$, and $F_{30} = 1$ then we recover the dilute gas formalism of Goldreich and Tremaine (1978) to order \mathbf{a} . See Section 2.2.9.

References

- [1] Abramowitz, M., Stegun, I. A., 1965. *Handbook of Mathematical Functions*. Dover, New York.
- [2] Albers, N., Spahn, F., 2006. The influence of particle adhesion on the stability of agglomerates in Saturn's rings. *Icarus*, **181**, 292-301.
- [3] Araki, S., 1988. The Dynamics of Particle Disks II. Effects of Spin Degrees of Freedom. *Icarus*, **76**, 182-198.
- [4] Araki, S., 1991. The Dynamics of Particle Disks III. Dense and Spinning Particle Disks. *Icarus*, **90**, 139-171.
- [5] Araki, S., Tremaine, S., 1986. The Dynamics of Dense Particle Disks. *Icarus*, **65**, 83-109.
- [6] Aranson, I. S., 2002. The world of the complex Ginzberg-Landau equation. *Reviews of Modern Physics*, **74**, 99-143.
- [7] Bhatnagar, P. L., Gross, E. P., Krook, M., 1954. A model for collisional processes in gases. I. Small amplitude processes in charged and neutral one-component systems. *Physical Review*, **94**, 511-525.
- [8] Binney, J., Tremaine, S., 1987. *Galactic Dynamics*. Princeton University Press, Oxford.

- [9] Borderies, N., Goldreich, P., Tremaine, S., 1985. A granular flow model for dense planetary rings. *Icarus*, **63**, 406-420.
- [10] Brahic, A., 1977. Systems of Colliding Bodies in a Gravitational Field: I - Numerical Simulation of the Standard Model. *Astronomy and Astrophysics*, **54**, 895-907.
- [11] Bridges, F., Hatzes A., Lin, D. N. C., 1984. Structure, Stability and Evolution of Saturn's Rings. *Nature*, **309**, 333-335.
- [12] Brilliantov, N. V., Pöschel, T., 2004. *Kinetic Theory of Granular Gases*. Oxford University Press, New York.
- [13] Carnahan, N. F., Starling, K. E., 1969. Equation of state for non-attracting rigid spheres. *Journal of Chemical Physics*, **51**, 635-636.
- [14] Chapman, S., Cowling, T. G., 1970. *The Mathematical Theory of Nonuniform Gases*, 3rd edition. Cambridge University Press, Cambridge, UK.
- [15] Colwell, J. E., Esposito, L. W., Sremcevic, M., Stewart, G. R., McClinck, W. E., 2007. Self-gravity wakes and radial structure of Saturn's B ring. *Icarus*, **190**, 127-144.
- [16] Devore, J. A., 1984. A pressure consistent BGY equation: Virial coefficients for rigid disks and spheres. *Journal of Chemical Physics*, **80**, 1304-1308.
- [17] Durisen, R. H., 1995. An instability in planetary rings due to ballistic transport. *Icarus*, **115**, 66-85.
- [18] Goertz, C.K., Morfill, G., 1988. A new instability of Saturn's rings. *Icarus*, **74**, 325-330.
- [19] Goldreich, P., Lynden-Bell, D., 1965. II. Spiral arms as sheared gravitational instabilities. *Monthly Notices of the Royal Astronomical Society*, **130**, 125-158.
- [20] Goldreich, P., Tremaine, S., 1978a. The Velocity Dispersion in Saturn's Rings. *Icarus*, **34**, 227-239.
- [21] Grad, H., 1949. On the kinetic theory of rarefied gases. *Communications on Pure and Applied Mathematics*, **2**, 331-407.
- [22] Hämeen-Anttila, K. A., 1978. An improved and generalized theory for the collisional evolution of Keplerian systems. *Astrophysics and Space Science*, **58**, 477-519.
- [23] Hämeen-Anttila, 1981. Quasi-equilibrium in collisional systems *Moon and the Planets*, **25**, 477-506.
- [24] Hämeen-Anttila, 1982. Saturn's rings and bimodality of Keplerian systems *Moon and the Planets*, **26**, 171-196.
- [25] Hämeen-Anttila, K. A., Salo, H., 1993. Generalised Theory of Impacts in Particulate Systems. *Earth, Moon, and Planets*, **62**, 47-84.
- [26] Hatzes, A. P., Bridges, F. G., Lin, D. N. C., 1988. Collisional properties of ice spheres at low impact velocities. *Monthly Notices of the Royal Astronomical Society*, **231**, 1091-1115.
- [27] Hatzes, A. P., Bridges, F., Lin, D. N. C., Sachtjen, S., 1991. Coagulation of Particles in Saturn's Rings: Measurements of the Cohesive Force of Water Frost. *Icarus*, **89**, 113-121.

- [28] Horn, L. J., Cuzzi, J. N., 1995. Characteristic Wavelengths of Irregular Structure in Saturn's B Ring. *Icarus*, **119**, 285-310.
- [29] Infeld, E., Rowlands, G., 1990. *Nonlinear Waves, solitons and chaos*. Cambridge University Press, Cambridge.
- [30] Jenkins, J. T., Richman, M. W., 1985. Grad's 13-moment System for a Dense Gas of Inelastic Spheres. *Archive for Rational Mechanics and Analysis*, **87**, 355-377.
- [31] Kato, S., 1978. Pulsational instability of accretion disks to axially symmetric oscillations. *Monthly Notices of the Royal Astronomical Society*, **185**, 629-642.
- [32] Latter, H. N., Ogilvie, G. I., 2006. The linear stability of dilute particulate rings. *Icarus*, **184**, 498-516.
- [33] Lin, D. N. C., Bodenheimer, P., 1981. On the Stability of Saturn's Rings. *The Astrophysical Journal*, **248**, L83-L86.
- [34] Lukkari, J., 1981. Collisional Amplification of Density Fluctuations in Saturn's rings. *Nature*, **292**, 433-435.
- [35] Lukkari, J., 1989. Velocity dispersion in particulate disks with size distribution. *Earth, Moon, Planets*, **44**, 207-218.
- [36] Marouf, E. A., Tyler, G. L., Zebker, H. A., Simpson, R. A., Eshleman, V. R., 1983. Particles Size Distributions in Saturn's Rings from Voyager 1 Radio Occultation. *Icarus*, **54**, 189-211.
- [37] McDonald, J. S. B., Hatzes, A., Bridges, F., Lin, D. N. C., 1989. Mass Transfer during Ice Particle Collisions in Planetary Rings. *Icarus*, **82**, 162-179.
- [38] Morishima, R., Salo, H., 2006. Simulations of dense planetary rings. *Icarus*, **181**, 272-291.
- [39] Mosqueira, I., (1996). Local simulations of Perturbed Dense Planetary Rings. *Icarus*, **122**, 128-152.
- [40] Porco, C. C. and 34 colleagues, 2005. Cassini Imaging Science: Initial Results on Saturn's Rings and Small Satellites. *Science*, **307**, 1226-1236.
- [41] Pöschel, T., Brilliantov, N. V., Schwager, T., 2002. Violation of Molecular Chaos in Dissipative Gases. Unpublished. arXiv: cond-mat/0210058 v1.
- [42] Ree, F. H., Hoover, W. G., 1967. Seventh virial coefficients for hard spheres and hard disks. *Journal of Chemical Physics*, **46**, 4181-4197.
- [43] Salo, H., 1987. Collisional evolution of rotating, non-identical particles. *Earth, Moon, and Planets*, **38**, 149-181.
- [44] Salo, H., 1991. Numerical Simulations of Dense Collisional Systems. *Icarus*, **90**, 254-270.
- [45] Salo, H., 1992a. Gravitational wakes in Saturn's rings. *Nature*, **359**, 619-621.
- [46] Salo, H., 1992b. Numerical simulations of dense collisional systems II. Extended distribution of particle sizes. *Icarus*, **96**, 85-106.
- [47] Salo, H., Karjalainen, R., 2003. Photometric modeling of Saturn's rings I. Monte Carlo method and the effect of nonzero volume filling factor. *Icarus*, **164**, 428-460.

- [48] Salo, H., Schmidt, J., Spahn, F., 2001. Viscous Overstability in Saturn's B Ring: I. Direct Simulations and Measurement of Transport Coefficients. *Icarus*, **153**, 295-315.
- [49] Savage, S. B., Jeffrey, D. J., 1981. The stress tensor in a granular flow at high shear rates. *Journal of Fluid Mechanics*, **110**, 255-272.
- [50] Schmidt, J., Salo, H., 2003. Weakly Nonlinear Model for Oscillatory Instability in Saturn's Dense Rings. *Physical Review Letters*, **90**, 061102, 1-4.
- [51] Schmidt, J., Salo, H., Spahn, F., Petzschmann, O., 2001. Viscous Overstability in Saturn's B-Ring: II. Hydrodynamic Theory and Comparison to Simulations. *Icarus*, **153**, 316-331.
- [52] Schmit, U., Tscharnuter, W. M., 1995. A Fluid Dynamical Treatment of the Common Action of Self Gravitation, Collisions and Rotation in Saturn's B-Ring. *Icarus*, **115**, 304-319.
- [53] Schmit, U., Tscharnuter, W. M., 1999. On the Formation of the Fine-Scale Structure in Saturn's B Ring. *Icarus* **138**, 173-187.
- [54] Shu, F. H., Stewart, G. R., 1985. The Collisional Dynamics of Particulate Disks. *Icarus*, **62**, 360-383.
- [55] Shukhman, I. G., 1984. Collisional dynamics of particles in Saturn's rings. *Soviet Astronomy*, **28**, 574-584.
- [56] Spahn, F., Schmidt, J., 2006. Hydrodynamic Description of Planetary Rings. *GAMM-Mitteilungen*, **29**, 115-140 .
- [57] Spahn, F., Schmidt, J., Petzschmann, O., 2000. Stability Analysis of a Keplerian Disk of Granular Grains: Influence of Thermal Diffusion. *Icarus*, **145**, 657-660.
- [58] Stewart, G. R., Lin, D. N. C., Bodenheimer, P., 1984. Collisional Transport Processes. In: Greenberg, R., Brahic, A. (eds). *Planetary Rings*. University of Arizona Press, Tucson, Arizona.
- [59] Supulver, K. D., Bridges, F. G., Lin, D. N. C., 1995. The Coefficient of Restitution of Ice Particles in Glancing Collisions: Experimental Results for Unfrosted Surfaces. *Icarus*, **113**, 188-199.
- [60] Supulver, K. D., Bridges, F. G., Tiscareno, S., Lievore, J., Lin, D. N. C., 1997. The Sticking Properties of Water Frost Produced under Various Ambient Conditions. *Icarus*, **129**, 539-554.
- [61] Tremaine, S., 2003. On the Origin of Irregular Structure in Saturn's Rings. *The Astronomical Journal*, **125**, 894-901.
- [62] Ward, W. R., 1981. On the Radial Structure of Saturn's Rings. *Geophysical Research Letters*, **8**, 641-643.
- [63] Weidenschilling, S. J., Chapman, C. R., Davis, D. R., Greenberg, R., 1984. Ring Particles: Collisional Interactions and Physical Nature. In: Greenberg, R., Brahic, A. (eds). *Planetary Rings*. University of Arizona Press, Tucson, Arizona.
- [64] Wisdom, J., Tremaine, S., 1988. Local Simulations of Planetary Rings. *The Astronomical Journal*, **95**, 925-940.
- [65] Zebker, H. A., Marouf, E. A., Tyler, G. L., 1985. Saturn's Rings: Particle

Size Distributions for Thin Layer Models. *Icarus*, **64**, 531-548.